Computations of Combustion-Powered Actuation for Dynamic Stall Suppression

Solkeun Jee*, Patrick O. Bowles, Claude G. Matalanis, Byung-Young Min, and Brian E. Wake,
United Technologies Research Center, East Hartford, CT

Tom Crittenden and Ari Glezer,
Georgia Institute of Technology, Atlanta, GA

ABSTRACT

A computational framework for the simulation of dynamic stall suppression with combustion-powered actuation (COMPACT) is validated against wind tunnel experimental results on a VR-12 airfoil. COMPACT slots are located at 10% chord from the leading edge of the airfoil and directed tangentially along the suction-side surface. Helicopter rotor-relevant flow conditions are used in the study. A computationally efficient two-dimensional approach, based on unsteady Reynolds-averaged Navier-Stokes (RANS), is compared in detail against the baseline and the modified airfoil with COMPACT, using aerodynamic forces, pressure profiles, and flow-field data. The two-dimensional RANS approach predicts baseline static and dynamic stall very well. Most of the differences between the computational and experimental results are within two standard deviations of the experimental data. The current framework demonstrates an ability to predict COMPACT efficacy across the experimental dataset. Enhanced aerodynamic lift on the downstroke of the pitching cycle due to COMPACT is well predicted, and the cycle-averaged lift enhancement computed is within 3% of the test data. Differences with experimental data are discussed with a focus on three-dimensional features not included in the simulations and the limited computational model for COMPACT.

NOTATION

C_D = aerodynamic drag coefficient
C_{Dp} = aerodynamic drag coefficient based on pressure
C_L = aerodynamic lift coefficient
C_M = aerodynamic moment coefficient
F^+ = non-dimensional pulse frequency, $f_{act} c/U_\infty$
$N_{\Delta t}$ = number of time steps
Ma = Mach number
P_r = pressure ratio
P_{act} = pressure boundary condition for actuator
$P_{act,out}$ = pressure at actuator outlet
P_∞ = freestream pressure
Re_c = chord-based Reynolds number, $U_\infty c/v$
T_{act} = time interval between two pulses
$T_{act,pulse}$ = pulse duration of actuation
T_{pitch} = period of pitching motion
Tu = turbulent intensity
U_∞ = freestream velocity

c = airfoil chord-length, inches
f_{act} = actuation frequency, $1/T_{act}$, Hz
f_{pitch} = pitching frequency, $1/T_{pitch}$, Hz
k = reduced frequency, $2\pi f_{pitch}c/(2U_\infty)$
s = span of lade model, inches
s_{act} = span of actuated portion of blade model, inches
t = dimensional time, seconds
t_o = beginning of pulse in COMPACT
-

t = convective time scale c/U_∞
x = streamwise coordinate, inches
y = cross-streamwise coordinate, inches

α = angle of attack
α_0 = mean angle of attack
α_1 = amplitude of angle of attack
Δy^+ = first wall-normal grid size in the viscous wall unit
φ = pitch cycle fractional phase
ρ = density
v = kinematic viscosity
ν = working variable in the Spalart-Allmaras model
θ_{slot} = angle of actuator slot with respect to airfoil surface

CFD = computational fluid dynamics
$\tilde{\text{COMPACT}}$ = computation-powered actuation
RANS = Reynolds-averaged Navier-Stokes
SA = Spalart-Allmaras turbulence model

INTRODUCTION

Dynamic stall occurs on the retreating side of a helicopter rotor and degrades performance in high-speed and high-thrust operations. As demand increases for higher speed and maneuverability, the need to control retreating-blade stall becomes more critical. Furthermore, unsteady aerodynamic effects due to dynamic stall cause adverse structural loads, excessive vibration, and component-life reduction.

Combustion-powered actuation (COMPACT) is a flow-control technology which provides a short-duration high-velocity jet from a miniaturized combustion chamber [1, 2]. Enhanced aerodynamic performance of COMPACT has

been successfully demonstrated for several stalled airfoils at low freestream Mach numbers near 0.1 [3, 4]. However, COMPACT performance at higher speed, e.g., Mach numbers from 0.2 to 0.4, was not well known. To address COMPACT effectiveness at relevant rotorcraft operating conditions, high-speed wind tunnel experiments [5] were conducted. Previous computational fluid dynamics (CFD) simulations [6, 7] helped to design the COMPACT actuators used in the high-speed experiments. The focus of this paper is to assess and adjust, if necessary, the CFD framework developed prior to the wind tunnel test by comparing CFD results with the newly acquired experimental data. The post-test comparisons are evaluated based on the ability of the simulations to predict key attributes of the flow-control impact on airfoil performance.

COMPUTATIONAL METHOD

EXPERIMENTAL CONDITIONS

A VR-12 blade model was tested in the NASA Icing Research Tunnel with and without COMPACT [5], as shown in Figure 1. The test section of the wind tunnel is 6 ft high, 9 ft wide, and 20 ft long [8]. The chord of the wing model is c=15 inches, and the wing spans from the floor to the ceiling s=68.5 inches. The pitch axis is located at $(x,y)_{pitch}$=(0.25, 0.0223c), midway between the pressure and suction sides of the airfoil, where the origin (x,y)=(0,0) is located at the leading edge of the airfoil. In the test section, the pitch axis is located at the mid width, 7.1c downstream from the beginning of the test section. The icing spray bar upstream of the test section yields a nominal turbulence intensity of Tu=1.2% in the test section for Ma=0.2-0.3 and a nominal flow angularity $\Delta\alpha = \pm0.6°$ for Ma=0.2-0.4 [8].

From the wind tunnel experiments, two configurations are the focus of the current study: (1) a clean leading edge (LE) configuration (Figure 1b) and the (2) COMPACT configuration (Figure 1c) [5]. Thirty-six individual COMPACT modules were used along the leading edge; the array of modules covers 33.1% of the wing span. One individual COMPACT module (shown in Figure 1d) spans 3.33%c (0.5 inch). A 0.0625-inch side wall divides individual modules. The COMPACT slot is located at x_{slot}=0.1c with an angle to the surface of $\theta_{slot} = 22°$, which was determined in the previous simulations [6]. The vanishing gap concept tested in the simulation [6] is used for the COMPACT side wall so that jets coming from individual modules merge on the actuated wing surface. The high-speed experiment [5] demonstrated significant enhancement of the aerodynamic lift beyond the nominal stall conditions, which was similarly observed in low-speed experiments [3, 4] and high-speed simulations [6, 7]. Refer to [5, 9] for a detailed description of the experimental conditions and test data.

COMPUTATIONAL CONDITIONS

Because 2D CFD was mainly used in the previous simulations for the COMPACT actuator design [6, 7], the main objective of this study is to validate the 2D CFD

framework. In line with the experimental conditions [5], the baseline airfoil is a VR-12 airfoil with a trailing-edge tab. The tab thickness is 0.005c, and the length is 0.05c. The tab is inserted to the 2% scaled-down, un-tabbed VR-12 airfoil with a slight modification on the airfoil profile near the junction of the tab and the airfoil. The coordinates of the tabbed VR-12 airfoil are included in the Appendix.

Computational grids are generated around the VR-12 airfoils with and without COMPACT. The clean airfoil without COMPACT was simulated in the previous studies [6] with grid convergence checks. The COMPACT geometry is introduced to the CFD domain with grids clustered around the slot exit (see Figure 2) without modifying the rest of the external flow grids. Whereas the COMPACT plenum is not included, the exact slot exit geometry is included in the current simulation. A 761x145 O-type grid is used for the airfoil, and a 145x129 grid for the slot. The first wall-normal grid point is located at $\Delta y^+ \leq 1$. The far-field boundary is located 50c away from the airfoil.

Rotor-relevant flow conditions are selected: the Mach numbers are Ma=0.2, 0.3, and 0.4. The corresponding Reynolds numbers are Re_c=1.7, 2.6, and 3.5 million, respectively. Four major cases are examined: (1) baseline steady airfoils, (2) baseline pitching airfoils, (3) a steady airfoil with COMPACT, and (4) a pitching airfoil with COMPACT. Flow conditions simulated for each case are listed in Table 1. The pitching motion was prescribed as $\alpha=\alpha_0+\alpha_1 sin(2kt/t_c)$, where the reduced frequency k is defined as $k=\pi f_{pitch}c/U_\infty$ and selected to be representative of rotor conditions on the retreating side in the range of Mach number Ma=0.2-0.4. The reference velocity is the freestream velocity U_∞, and the reference time is the convective time scale t_c=c/U_∞. The pulse duration of COMPACT is $T_{act,pulse}$=0.7msec. The non-dimensional actuation frequency is defined as $F^+ = f_{act}c/U_\infty$ where the time between two pulses, $T_{act,}$ determines the actuation frequency, i.e., $f_{act} = 1/T_{act}$. The range of f_{act} is $72 \leq f_{act} \leq 212$ Hz in this paper, as found in the experiment. Experimental data of the peak pressure ratio $P_{r,peak}$ due to the combustion process in the chamber is used for the COMPACT simulations. In the test, the pressure ratio was measured at the steady airfoil condition of Ma=0.3 and α=18° for selected frequencies f_{act}=53, 106, 159, 212Hz. The pressure ratio is assumed to be a function of f_{act} only because of the limited measurement. For other frequencies considered in CFD, $P_{r,peak}$ is linearly interpolated from this dataset. This unavoidable assumption is discussed in the section Computational Results with comparison of simulations to experimental data.

CFL3D is used for the simulations with the full Navier-Stokes solver option and the Spalart-Allmaras (SA) turbulence model [10]. Since the turbulence intensity is high, Tu=1.2% in the test, the fully-turbulent flow condition, $\tilde{v}_\infty = 4\nu$, is used for the turbulence model at the far field. The third-order, upwind-biased Roe scheme is used for Euler fluxes, and the second-order central scheme is used for viscous fluxes. Unsteady RANS is used for all the reported

simulations in this paper. The second-order implicit approximate-factorization method is used for the time marching with the pseudo time sub-iteration method. Time step parameters tested in the study are listed in Table 1. Additional time steps Δt are tested to check temporal convergence in selected cases, and the smallest time step size in each case is used for the results in this paper. The number of the time steps per pitch $N_{\Delta t}/T_{pitch}$ and the pulse duration $N_{\Delta t}/T_{act,pulse}$ are included in Table 1. The Courant-Friedrichs-Lewy (CFL) number for sub-iterations is 5, and the number of sub-iterations in all the cases is 30 for sufficient convergence per time step. For pitching conditions, cycle-to-cycle convergence was achieved after the first three pitch cycles.

A pressure condition P_{act} is applied at the actuator boundary where the slot meets the combustion chamber, as shown in Figure 2c. Experimental data of the pressure ratio, $P_r(t)$, are based bench-top test data. CFD without actuation indicates that the chamber pressure is similar to the pressure outside of the actuator $P_{act,out}$, particularly the pressure on the airfoil surface upstream of the slot exit. It is expected that the chamber pressure just before the next pulse $P_{act,0}$ is close to the pressure at the actuator outlet $P_{act,out}$. Consequently, the following pressure boundary condition Eq. 1 is obtained.

$$P_{act}(t) = P_r(t)P_{act,0} \quad (1)$$

The reference pressure $P_{act,0}$ holds its value only during the pulsation. It is updated with the extrapolated pressure on the boundary just before the next pulse starts. Note that this is a major change in the boundary condition, compared to the previous studies [6, 7] where the free-stream pressure is used for the reference pressure; from close examination of the CFD and test data, the previous assumption did not well represent the actual test conditions. This is because the free-stream pressure is higher than the actuator outlet pressure on the suction surface $P_\infty > P_{act,out}$ for conditions considered here. The following cosine function is used for $P_r(t)$ for $0 \le t - t_o \le T_{act,pulse}$

$$P_r = \frac{P_{r,peak}}{2}\left[\cos\left(2\pi\frac{t - t_0}{T_{act,pulse}} - \pi\right) + 1\right] \quad (2)$$

where t_o is the beginning of the pulse. When the pressure is set to $P_{act}(t)$, the density, ρ_{act}, and the velocity, $\vec{u}_{act}$, are extrapolated. This approach is similar to the original CFL3D boundary type 2002 [11]; a notable difference is the time-dependent pressure.

In the initial post-test validation cases, it was observed that the flow can exit the CFD domain through the actuator boundary due to the pressure fluctuation on the suction-side surface driving fluid into the slot. The pressure oscillation is generated by the nominal shedding, which leads to outflow at the actuator boundary when $P_{act,0} < P_{act,out}$. Such outflow caused unphysical solutions. To remedy this numerical problem, the jet velocity is set to zero between pulses. The pressure is extrapolated, and the density is set so

that the temperature at the actuator boundary is equal to the free-stream value.

The complete actuator boundary condition is written as Eqs. 3 and 4. The wall velocity, $\vec{u}_{wall}$, is set by the airfoil motion. At the actuator boundary, the SA model boundary condition was set to $\tilde{\nu}_{act} = 4\nu$.

$$\text{For } t_o \le t \le t_o + T_{act,pulse}, \quad \begin{cases} \rho_{act}: \text{extrapolated} \\ \vec{u}_{act}: \text{extrapolated} \\ P_{act} = P_r(t)P_{act,0} \end{cases} \quad (3)$$

$$\text{For } t_o + T_{act,pulse} < t < T_{act}, \quad \begin{cases} \rho_{act} = \rho_\infty(P_{act}/P_\infty) \\ \vec{u}_{act} = \vec{u}_{wall} \\ P_{act}: \text{extrapolated} \end{cases} \quad (4)$$

COMPUTATIONAL RESULTS

The four major cases are simulated and computational results are compared with experimental data. In this paper, the baseline includes the clean VR-12 airfoil without the actuator and the modified VR-12 with the actuator but no actuation. For the baseline and COMPACT cases, both steady and pitching airfoils are considered.

BASELINE STEADY AIRFOILS

Steady airfoils were simulated for three Mach numbers Ma=0.2, 0.3, and 0.4, as shown in Figure 3. The aerodynamic lift C_L, drag C_D, and moment C_M agree well with the experimental data for the clean airfoil. The slightly over-predicted lift in the linear-lift region could be related to the nominal flow angularity variation, $\Delta\alpha = \pm0.6°$, in the test section, which is not captured in the current CFD. The stall angle for the three Mach numbers is predicted slightly larger than that measured in the test. A well-known RANS limit for flow separation [12] may contribute to the slight delay of stall in the computations. In this paper, the CFD drag is the total drag, whereas the experimental drag is the pressure drag only.

When the actuator geometry, i.e., the slot, is incorporated in the modified airfoil, CFD results indicate negligible differences in the aerodynamic forces between the clean and the modified VR-12 airfoil across the Mach numbers and the angles of attack studied. The experimental data indicates that the nominal steady stall behavior could be significantly altered by the modified airfoil. The difference is clear for $Ma = 0.4$, and it is noticeable for $Ma = 0.2$ in the lift and moment profiles (Figure 3). Based on the experiments, the modified airfoil tends to yield a sharper stall behavior compared to the clean airfoil. Such differences could be related to slight modifications in the airfoil leading-edge (LE) due to installation of the actuator assembly. Any LE modifications potentially related to the hardware fabrication are not modeled in the current computations.

Figure 4 compares the CFD and experimental pressure profiles. Good agreement is observed. For small angles of attack before stall, $\alpha \le 16°$, the predicted suction pressure peak is lower than the test. The increased suction yields the higher lift in Figure 3. As previously noted, the apparent

flow angle near the leading edge could be slightly lower than the geometric angle of attack due to the flow angularity variation measured in the test section. For angles beyond stall, $\alpha \geq 18°$, CFD provides flattened profiles on the suction side, which was similarly observed in the experiment.

Flow fields are compared to particle-image velocimetry (PIV) data for angles beyond the stall, as shown in Figures 5 and 6. The recirculation region is well captured in the current computations and the size is comparable to the test data. For several stall conditions, e.g. $\alpha \geq 20°$, the current CFD shows an additional vortical structure near the trailing edge which is not shown in the PIV data. This may be related to the 2D constraint of the current simulations and any 3D effects in the test not captured here. The mixing of the separating shear layer is under-predicted in the current simulations, which is expected from the RANS limit [13]. Overall, the current CFD provides reasonable prediction of the aerodynamic forces, pressure profiles, and flow field over the range of Mach numbers and angles of attack tested.

BASELINE PITCHING AIRFOILS

CFD simulations were conducted for several experimental pitching conditions. Three Mach numbers, Ma=0.2, 0.3, and 0.4, are simulated with various combinations of prescribed pitching angle $\alpha(t)$ and reduced frequency, k. The simulated and tested conditions are listed in Table 1. Three types of experimental data are plotted in Figures 7-11. The average experimental force coefficient loops were obtained from the ensemble average of 64 pitching cycles. Each cycle has 512 samples for Ma=0.2 and 128 samples for $Ma \geq 0.3$. Individual data points are included and shown as grey markers. The standard deviation of the integrated loads, σ, is obtained for each phase of the pitching motion in the experimental data; this is used to plot $\pm 2\sigma$ variance lines (dashed black lines) from the ensemble mean. Last, the CFD data is plotted in red. Cycle-to-cycle convergence is achieved in the current simulations after the initial three cycles.

Overall, the agreement between the CFD and the experimental average data is good, and most of the difference is within the range of $\pm 2\sigma$, indicating that the CFD provides a plausible prediction of the dynamic stall behaviors observed in the test. Similar to the steady airfoil results, the aerodynamic lift at moderate angles is slightly higher than the experimental value, particularly during the up-stroke. The flow angularity variation $\Delta\alpha = \pm 0.6°$ in the test section could cause the apparent angle α to be slightly different from the target value, yielding the visual difference in lift. The drag qualitatively compares well to the experiments.

The moment also, in general, agrees well with the experimental data. Comparison of the moment peak, a good indicator of the stall vortex strength, with the experimental data shows that the absolute value of the adverse moment peak is often over-predicted in the simulations. The phase prediction of the peak is significantly better. Current 2D constraint could cause a stronger 2D stall vortex in the

simulations, whereas the stall vortex in the experiments could be altered by any 3D flow features.

The pressure profiles at 16 phases of the pitching motion are compared with the experimental average data (see Figures 12-15). Only four pitching conditions are considered here at Ma=0.2 and k=0.07. For the light dynamic stall pitching condition of $\alpha = 10 \pm 8°$ (Figure 12), the pressure profiles match well with the experiments. As the dynamic stall becomes more severe, differences are noticeable around the peak angle when the phase is $\phi = 1/2$. In Figure 13 ($\alpha = 10 \pm 10°$), the experimental data indicates that the flow separates from the airfoil suction side near x/c=0.2 at $\phi = 1/2$; CFD provides well-attached flow on the suction side until $\phi = 1/2$. The vortex near the trailing edge at $\phi = 9/16$ in the simulation is associated with the large negative moment peak in Figure 7. The trailing edge vortex is more apparent in the simulation for more severe dynamic stall conditions of $\alpha = 15 \pm 8°$ (Figure 14) and $\alpha = 15 \pm 10°$ (Figure 15) when the phase is $7/16 \leq \phi \leq 9/16$. The $\alpha = 10 \pm 10°$ case shown in Figure 13 is further studied through the stacked surface pressures versus the pitching motion phase in Figure 16. Five selected pressure ports are used for both the suction and pressure sides of the airfoil. The stacked pressure for the suction side indicates that the flow separation is slightly delayed in the simulation by $\phi \simeq 1/32$. The abrupt oscillations seen for $1/2 < \phi < 5/8$ for the trailing-edge pressure measurements on both airfoil sides indicate the trailing-edge vortex.

The Mach contour from the simulation is compared to the PIV data in Figure 17. As the airfoil pitches up, the boundary layer grows on the suction side and separates. The separation occurs slightly earlier in the experiment (before $\alpha = 19.85°$ on the upstroke), compared to the simulation (after $\alpha = 19.85°$ on the upstroke). After the dynamic stall vortex fully detached from the airfoil, the recirculation region is well predicted in the simulation at $\alpha = 19.27°$ on the downstroke. However, the simulation predicts additional vortical structure near the trailing edge that was not observed in the PIV. As the airfoil pitches down, both CFD and PIV give similar accounts of the reduction in the recirculation region's time dependent nature.

STEADY AIRFOIL WITH COMPACT

The modified VR-12 airfoil with COMPACT is simulated for fixed angles of attack. The nondimensional actuation frequency is F^+=0.4 for the steady airfoil. The CFD predicts that COMPACT does not significantly change the aerodynamic lift or pitching moment before the nominal stall angle, as observed in the experimental data and compared in Figure 18. The lift enhancement is predicted well up to $\alpha = 18° - 19°$ for $Ma = 0.2$ and 0.3. However, for higher angles, CFD over-predicts the lift enhancement across the Mach numbers. A noticeable reduction in the drag was obtained in computations before the nominal stall, which was not achieved in the experimental pressure drag. At high angles, e.g. $\alpha = 20°$, the actuation tends to yield a

larger drag value compared to the un-actuated case in both the simulation and the experiment.

Pressure profiles were compared for three selected angles at Mach=0.3, as shown in Figure 19. At $\alpha = 16°$ and 18°, CFD pressure profiles agree well with the experimental profiles with and without actuation. At the higher angle, $\alpha = 20°$, CFD predicts significant lift enhancement on the aft suction side, which creates a large nose-down moment. The experimental pressure profile at $\alpha = 20°$ is similar to that of $\alpha = 18°$; and no significant difference in the aerodynamic forces is observed between these two angles. There is a notch in the CFD lift profile around $\alpha = 18°$ which was not observed in the experiments.

Several factors could lead to the difference between the current CFD and the experiments. The assumption of $P_{r,peak} = P_{r,peak}(f_{act}$ only) could be limited. $P_{r,peak}$, which was measured at $\alpha = 18°$ and Ma=0.3, could depend on external flow conditions such as α and Mach which influences the operating pressure near the slot outlet on the suction side. More measurements would help to better construct $P_{r,peak}$ for the various flow conditions. The discrepancy between CFD and experiment, particularly at high angles of attack, may be related to the limits of the current 2D CFD approach. Analysis described in [5] and [9] indicated that the low actuated aspect ratio, $s_{act}/c = 1.51$, can induce 3D flow which significantly impacts the calculated sectional aerodynamic forces, particularly drag, and to lesser extent, moment. The capability of the one-equation SA RANS model for modeling multi-scale flow features associated with COMPACT and the stall phenomena is also open to question.

Flow fields following the actuation trigger are compared to the PIV data, as shown in Figures 20-23. The actuation significantly reduces the low Mach region on the suction side, forcing high momentum flow toward the VR-12 upper surface; the flow interaction is well captured in the simulation for moderate stall conditions where $\alpha \simeq \alpha_{stall} + 2°$. Figures 20 and 21 highlight these angles of attack. The variable t' is the time after the beginning of the actuation, $t' = t - t_o$. For severe stall conditions such as $\alpha \simeq \alpha_{stall} + 4°$, as shown in Figures 22 and 23, the simulation shows additional vortical structures in the recirculation region near the trailing edge before the actuation begins at $t' = 0$. Consequently, the jet from COMPACT dynamically interacts with the recirculation in the CFD, which may generate dynamic-stall-like phenomena, yielding higher lift enhancement than the experiments.

PITCHING AIRFOIL WITH COMPACT

CFD simulations were conducted for selected experimental conditions for pitching airfoils. The actuator frequency $F^+ = 0.4$ was used for the three Mach numbers. An additional pulse frequency, $F^+ = 0.8$, is compared for Ma = 0.3. Phase-averaged aerodynamic forces were obtained using ten pitch cycles. It was observed that more than six cycles are enough for converged statistics.

Computational aerodynamic forces were compared with the relevant experimental data.

For Ma=0.2, Figure 24 and Figure 25 compare the computational results with the test data for two pitching frequencies, $k = 0.07$ (Figure 24) and 0.1 (Figure 25). The CFD predicts a large lift enhancement in the first half of the down-stroke, as observed in the experiments. The negative moment peak shifts to approximately one degree later in the down-stroke, which is also noticed in the experimental data. The drag peak was reduced in CFD. As stated previously, experimental drag was modified significantly by 3D effects, and therefore, quantitative drag comparison is not pursued here.

Two actuator frequencies $F^+ = 0.4$ and 0.8, were simulated with the pitching frequency $k = 0.1$, as shown in Figure 25. Similar to the $k = 0.07$ case, the downstroke lift increase was well-predicted. Both CFD and experiment indicate larger lift enhancement for the higher actuator frequency. CFD suggests a large reduction in the negative peak moment for both actuator frequencies, whereas the experimental data records noticeable reduction only for the higher frequency $F^+ = 0.8$. Similar to the $k = 0.07$ case, the current computations predict a large reduction in the drag peak with COMPACT.

For Ma=0.3, computational results were compared with experimental data for two pitching frequencies. Figure 26 compares the $k = 0.07$ data and Figure 27 compares $k = 0.1$. The performance of COMPACT with $F^+ = 0.4$ was well captured for both cases in the lift enhancement during the down-stroke. Since the current 2D CFD was not able to capture the baseline moment peak, predicting the moment modulation due to COMPACT was also challenging. For both pitching frequencies, CFD provides reductions in the moment peak amplitude, whereas the experimental data shows a noticeable reduction for only the higher frequency $k = 0.1$ case.

The COMPACT performance in the lift was also reasonably modeled with the enhanced lift in the down-stroke for Ma=0.4, as shown in Figure 28. Both CFD and experiments show no significant change in the up-stroke. The moment stall was not significantly altered by COMPACT in either the CFD or the experiment. Based on the CFD and experimental studies for $k = 0.07$ across the Mach number range, it is expected that COMPACT is more effective at lower Mach dynamic stall, e.g., the $Ma = 0.2$ case.

Among the combination of the pitching and the actuation conditions, CFD predicts well the undulation in the hysteresis loops in the down-stroke for the case of Ma=0.3, k=0.07, and F^+=0.4, as shown in Figure 29. Individual experimental data are included in the plot. The difference between the CFD and the experimental averaged data is within the standard deviation range of $\pm 2\sigma$ of the experimental forces. This observation highlights the randomness of dynamic stall as shown in experiments, where cycle-to-cycle differences are significant.

In the aerodynamic design [6], several metrics were used for the analysis of the overall COMPACT benefit. One key parameter is the change in the mean lift $C_{L,avg}$ due to the actuation,

$$\Delta C_{L,avg} = \left(C_{L,avg,COMPACT} - C_{L,avg}\right)/C_{L,avg} \ (\%). \quad (5)$$

As expected from the lift hysteresis modification, the enhancement in the mean lift per pitch cycle was well-predicted by the CFD. Figure 30 compares experimental and computational values for this key metric. The maximum difference between the computational and the experimental $\Delta C_{L,avg}$ is approximately 3%, $\Delta C_{L,avg,max} = \left|\Delta C_{L,avg,CFD} - \Delta C_{L,avg,EXP}\right|_{max} \simeq 3\%$.

CONCLUSIONS

The presented 2D CFD framework was extensively compared against the wind tunnel test data. Speeds relevant to rotorcraft retreating blade stall were chosen Ma=0.2-0.4 with a range of the reduced frequency k=0.07-0.1. In contrast with the pre-test CFD [6], the presented post-test CFD activity involved modifications in the computational method for the actual slot geometry and the COMPACT parameters used in high-speed tests. The actuator boundary condition was modified to better represent the pressure rise in the actuator.

Computational results for baseline airfoils were compared to experimental data, including the aerodynamic forces and moment, pressure profiles, and flow fields. Good agreement to the experiments was achieved across the Mach numbers and angles of attack for the airfoil at static conditions. Unsteady forces on pitching airfoils were also well-predicted by the current computations. The series of CFD baseline validation cases provided confidence to the subsequent study with COMPACT.

Good agreement with experimental data was achieved for the modified VR-12 airfoil with COMPACT in both the steady and pitching conditions. The lift enhancement from COMPACT was particularly well captured. The mean lift improvement per pitch cycle agrees well with the experimental values. Although it is challenging for the current 2D CFD method to predict details in unsteady aerodynamic forces due to COMPACT, this study indicates that the current computational method is able to predict the overall benefit of COMPACT on the aerodynamic lift.

Impact of COMPACT on the drag and moment shows noticeable differences to the experiments. This is primarily because of 3D effects associated with the limited spanwise extent of the actuated region, but could also be related to detailed flow features not captured well in the current 2D CFD. The impact of the experimental part-span actuation will be better captured with 3D RANS CFD. Detailed turbulence structures associated with COMPACT and the stall vortex would be better modeled with higher-fidelity approaches such as large-eddy simulation. Furthermore, better definition of actuator parameters, particularly in terms

of how the actuators will perform when subjected to full Mach number, pitching conditions, and the operating pressure on the suction surface (which is difficult to determine prior to tests) could improve the fidelity of the simulations.

Author contact: Solkeun Jee, jees@utrc.utc.com

REFERENCES
1. Crittenden, T., Glezer, A., Funk, R., and Parekh, D., *Combustion-Driven Jet Actuators for Flow Control*, in *31st AIAA Fluid Dynamics Conference and Exhibit*. 2001: Anaheim, CA.
2. Crittenden, T., Warta, B., and Glezer, A., *Characterization of Combustion Powered Actuators for Flow Control*, in *3rd AIAA Flow Control Conference*. 2006: San Francisco, CA.
3. Brzozowski, D., Woo, G., Culp, J., Glezer, A., *Transient Separation Control using Pulse-Combustion Actuation*. AIAA Journal, 2010. **48**: p. 2482-2490.
4. Woo, G., Crittenden, T., and Glezer, A., *Transitory Control of a Pitching Airfoil using Pulse Combustion Actuation*, in *4th Flow Control Conference*. 2008: Seattle, WA.
5. Matalanis, C.G., Bowles, P. O., Lorber, P., Crittenden, T., Glezer, A., Schaeffler, N., Min, B., Jee, S., Wake, B. E., *High-Speed Experiments on Combustion-Powered Actuation for Dynamic Stall Suppression*, in *AHS 72nd Annual Forum*. 2016: West Palm Beach, FL.
6. Jee, S., Matalanis, C.G., Min, B.Y., Bowles, P.O., Wake, B.E., Crittenden, T., Glezer, A., *Comptutaions of Dynamic Stall Control with Combustion-Powered Actuation*, in *AHS 71st Annual Forum*. 2015: Virginia Beach, VA.
7. Matalanis, C.G., Min, B.-Y., Bowles, P. O., Jee, S., Wake, B. E., Crittenden, T., Woo, G., and Glezer, A., *Combustion-Powered Actuation for Dynamic-Stall Suppression: High-Mach Simulations and Low-Mach Experiments*. AIAA Journal, 2015. **53**(8): p. 2151-2163.
8. Pastor-Barsi, C., Allen Arrington, E., *Aero-Thermal Calibration of the NASA Glenn Icing Research Tunnel (2012 Tests)*. 2013: NASA/CR-2013-217812.
9. Matalanis, C.G., Bowles, P. O., Jee, S., Min, B., Kuczek, A. E., Croteau, P. F., Wake, B. E., Crittenden, T., Glezer, A., Lorber, P., Schaeffler, N., *Dynamic Stall Suppresion Using Combustion-Powered Actuation (COMPACT)*. 2016: NASA/CR, submitted.

10. Spalart, P.R., and Allmaras, S. R., *A One-Equation Turbulence Model for Aerodynamic Flows.* Recherche Aerospatiale, 1994. **1**.
11. Rumsey, C. *CFL3D Version 6.6.* Last updated: 03/29/2013; Available from: http://cfl3d.larc.nasa.gov/.
12. Slotnick, J., Khodadous, A., Alonso, J., Damofal, D., Gropp, W., Lurie, E., Marviplis, D., *CFD Vision 2030 Study: A Path to Revolutionary Computational Aerosciences.* 2014: NASA/CR-2014-218179.
13. Muppidi, S., Mahesh, K., *Direct Numerical Simulation of Round Turbulent Jets in Crossflow.* Journal of Fluid Mechanics, 2007. **573**(3): p. 59-82.

APPENDIX

Table A.1 Airfoil and COMPACT slot coordinates

Suction Side		Suction Side (continuous)		Pressure Side	
x/c	y/c	x/c	y/c	x/c	y/c
0.0000	0.0000	0.6370	0.0537	0.0000	0.0000
0.0002	0.0033	0.6661	0.0498	0.0005	-0.0026
0.0010	0.0069	0.6946	0.0457	0.0024	-0.0053
0.0025	0.0107	0.7223	0.0416	0.0058	-0.0079
0.0046	0.0146	0.7492	0.0374	0.0105	-0.0101
0.0074	0.0186	0.7751	0.0333	0.0167	-0.0123
0.0109	0.0227	0.8000	0.0292	0.0247	-0.0143
0.0152	0.0267	0.8238	0.0251	0.0347	-0.0161
0.0201	0.0308	0.8464	0.0212	0.0471	-0.0176
0.0259	0.0349	0.8679	0.0173	0.0624	-0.0192
0.0324	0.0390	0.8882	0.0136	0.0810	-0.0209
0.0398	0.0430	0.9073	0.0099	0.1035	-0.0226
0.0480	0.0468	0.9252	0.0064	0.1305	-0.0242
0.0572	0.0506	0.9420	0.0030	0.1624	-0.0258
0.0674	0.0541	0.9574	0.0015	0.1995	-0.0272
0.0787	0.0574	0.9690	0.0014	0.2419	-0.0285
0.0889	0.0599	0.9774	0.0014	0.2896	-0.0295
0.0936	0.0609	0.9837	0.0014	0.3419	-0.0303
0.0977	0.0618	0.9883	0.0014	0.3979	-0.0305
0.1000	0.0622	0.9919	0.0014	0.4565	-0.0303
0.1023	0.0627	0.9946	0.0014	0.5161	-0.0298
0.1077	0.0636	0.9967	0.0014	0.5751	-0.0288
0.1149	0.0648	0.9983	0.0013	0.6320	-0.0274
0.1222	0.0658	0.9994	0.0005	0.6853	-0.0256
0.1294	0.0667	1.0000	-0.0008	0.7343	-0.0236
0.1367	0.0675	**Slot**		0.7781	-0.0215
0.1454	0.0684	x/c	y/c	0.8165	-0.0192
0.1514	0.0689	0.0977	0.0618	0.8497	-0.0168
0.1617	0.0697	0.0965	0.0611	0.8779	-0.0143
0.1790	0.0709	0.0951	0.0602	0.9015	-0.0117
0.1988	0.0719	0.0930	0.0589	0.9210	-0.0091
0.2199	0.0726	0.0911	0.0575	0.9370	-0.0066
0.2421	0.0731	0.0889	0.0560	0.9500	-0.0044
0.2655	0.0735	0.0862	0.0540	0.9637	-0.0036
0.2900	0.0736	0.0841	0.0526	0.9735	-0.0036
0.3156	0.0735	0.0875	0.0491	0.9808	-0.0036
0.3422	0.0733	0.0890	0.0510	0.9862	-0.0036
0.3697	0.0728	0.0911	0.0535	0.9902	-0.0036
0.3980	0.0721	0.0926	0.0555	0.9933	-0.0036
0.4270	0.0710	0.0941	0.0572	0.9957	-0.0036
0.4565	0.0697	0.0954	0.0584	0.9975	-0.0036
0.4865	0.0679	0.0964	0.0591	0.9989	-0.0031
0.5167	0.0659	0.0976	0.0598	0.9997	-0.0022
0.5471	0.0634	0.0997	0.0611	1.0000	-0.0008
0.5773	0.0605	0.1013	0.0621		
0.6073	0.0573	0.1023	0.0627		

Table 1 Flow conditions for four major cases with time step parameters

Case	Ma	α_0	α_1	k	F^+	$P_{r,peak}$	$\Delta t/t_c$	$N_{\Delta t}/T_{pitch}$	$N_{\Delta t}/T_{act,pulse}$
Baseline Steady Airfoils	0.2	$0 \le \alpha_0 \le 20$					0.0078		
	0.3	$0 \le \alpha_0 \le 25$	-	-	-	-	0.0078, 0.016	-	-
	0.4	$0 \le \alpha_0 \le 20$					0.0078		
Baseline Pitching Airfoils	0.2	10, 15	8, 10	0.07			0.0056, 0.011		
				0.1			0.0039, 0.0078		
	0.3	8, 10, 15	8, 10	0.07	-	-	0.0056, 0.011	4000, 8000	-
				0.1			0.0039, 0.0078		
	0.4	8, 10 10	5, 8 10	0.07			0.0056, 0.011		
Steady Airfoil with COMPACT	0.2	$10 \le \alpha_0 \le 20$	-	-	0.4	2.40	0.0039	-	32
	0.3				0.4	2.27			48
	0.4				0.4	1.91			64
Pitching Airfoil with COMPACT	0.2	10	10	0.07	0.4	2.40	0.0056	8000	22
				0.1	0.4	2.40	0.0039, 0.0078	4000, 8000	16, 32
					0.8	1.71			
	0.3	10	10	0.07	0.4	2.27	0.0056	8000	33
				0.1	0.4	2.27	0.0039, 0.0078	4000, 8000	24, 48
	0.4	10	10	0.07	0.4	1.91	0.0056, 0.011		22, 45
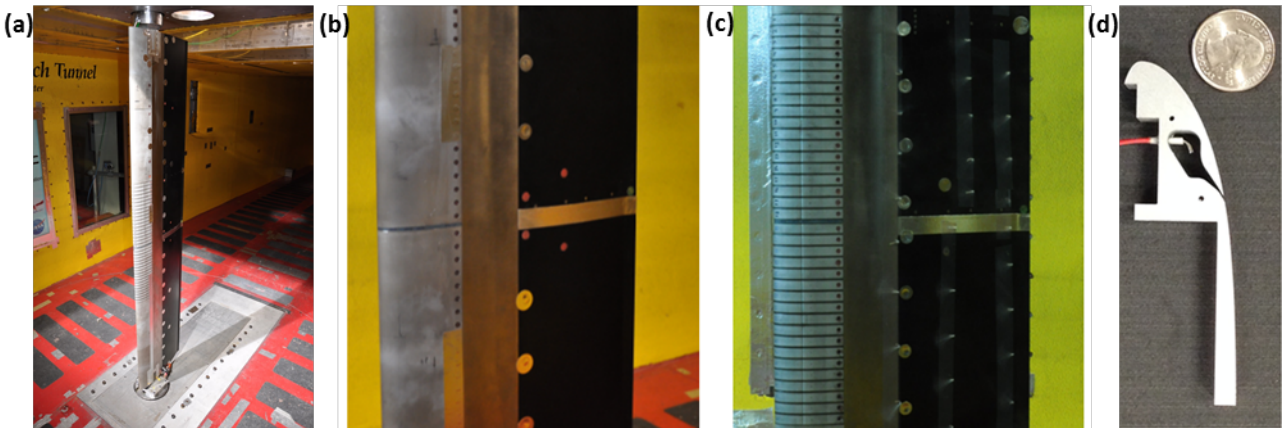
Figure 1. Wind tunnel test configuration: (a) VR-12 model installed in the NASA Icing Research Tunnel; (b) clean LE configuration; (c) COMPACT installation; and (d) COMPACT module [5].
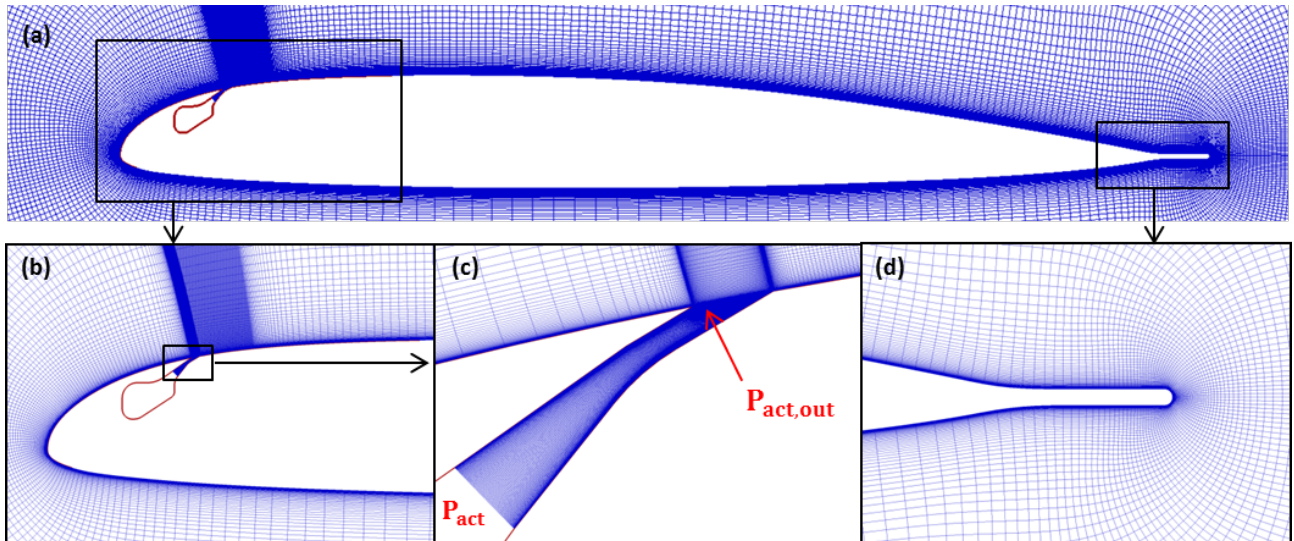
Figure 2. Grid around the modified VR-12 airfoil with the COMPACT slot.
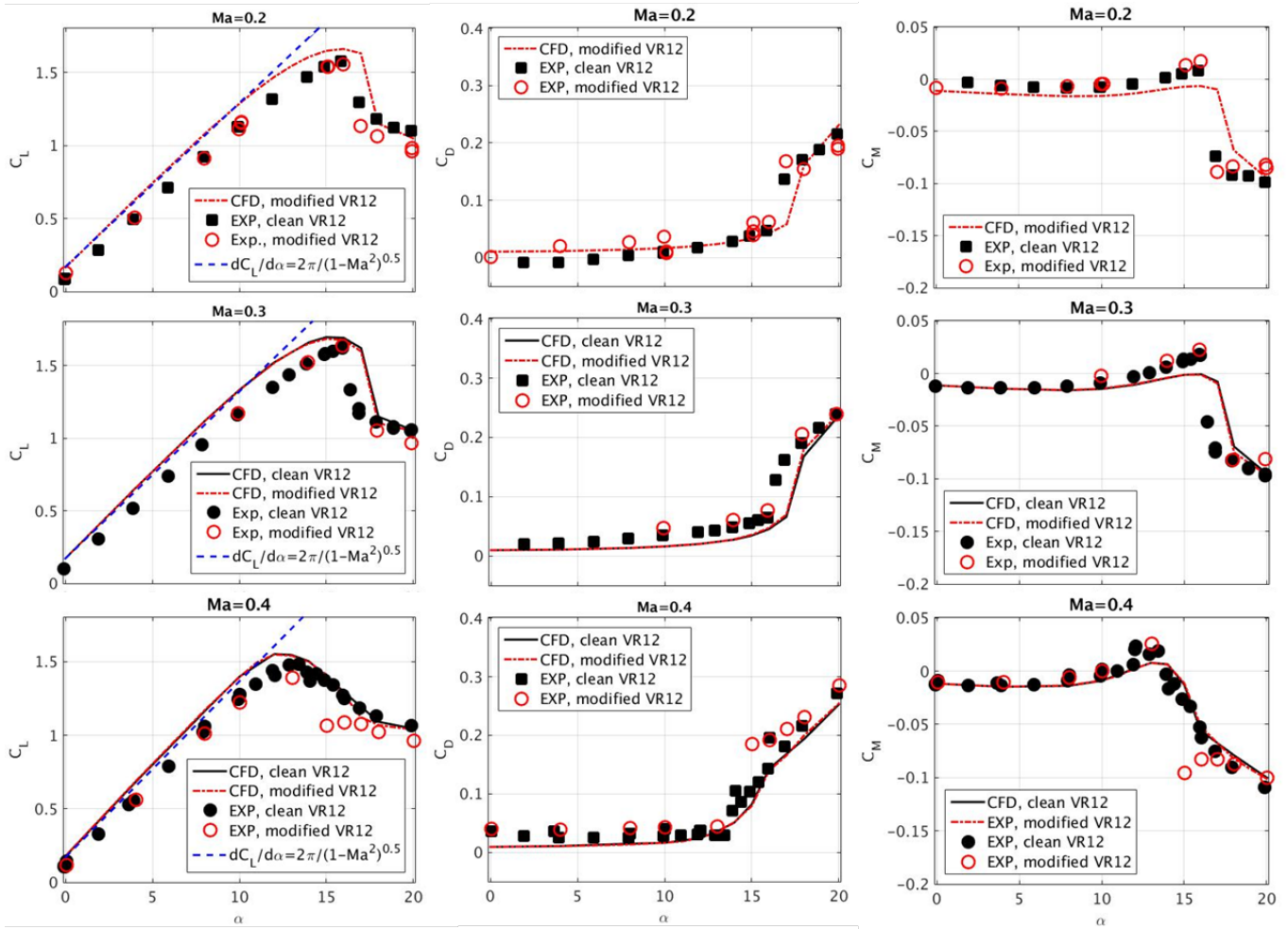
Figure 3. Aerodynamic forces for the baseline steady airfoils. *Ma*=0.2, 0.3 and 0.4.
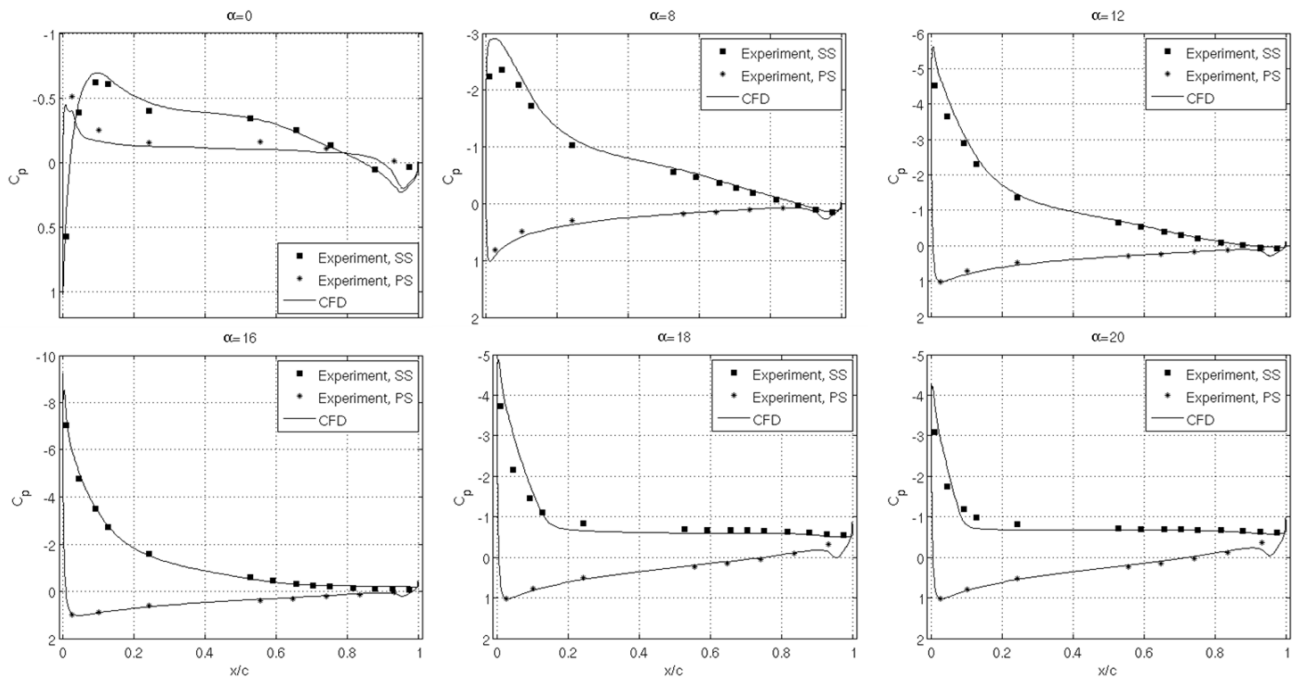
Figure 4. Pressure profiles for the baseline steady airfoil. *Ma*=0.3 [6].
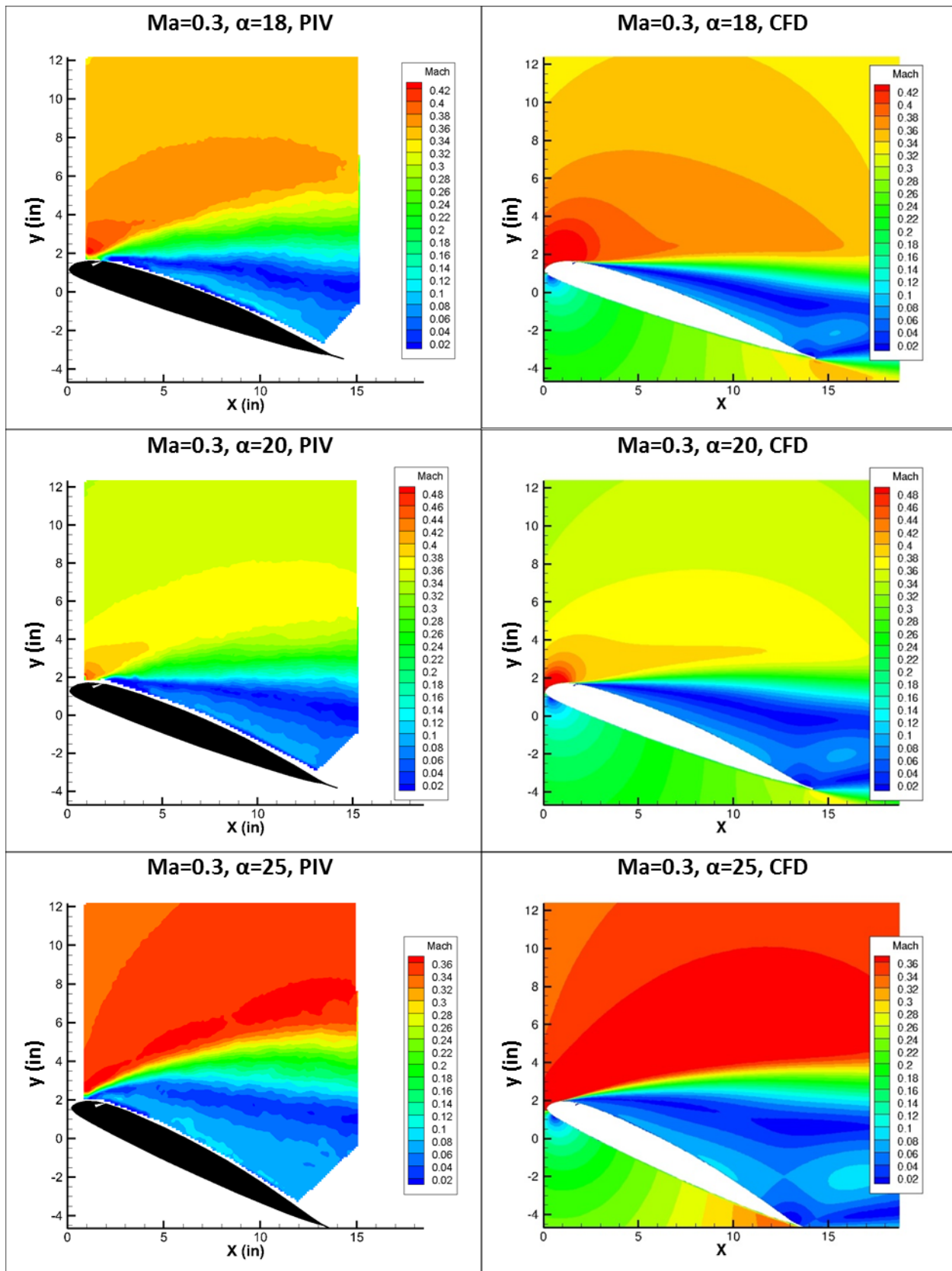
Figure 5. **Velocity fields for the baseline steady airfoil.** *Ma*=0.3. α=18 (top), 20 (middle) and 25° (bottom). PIV (left) and CFD (right).
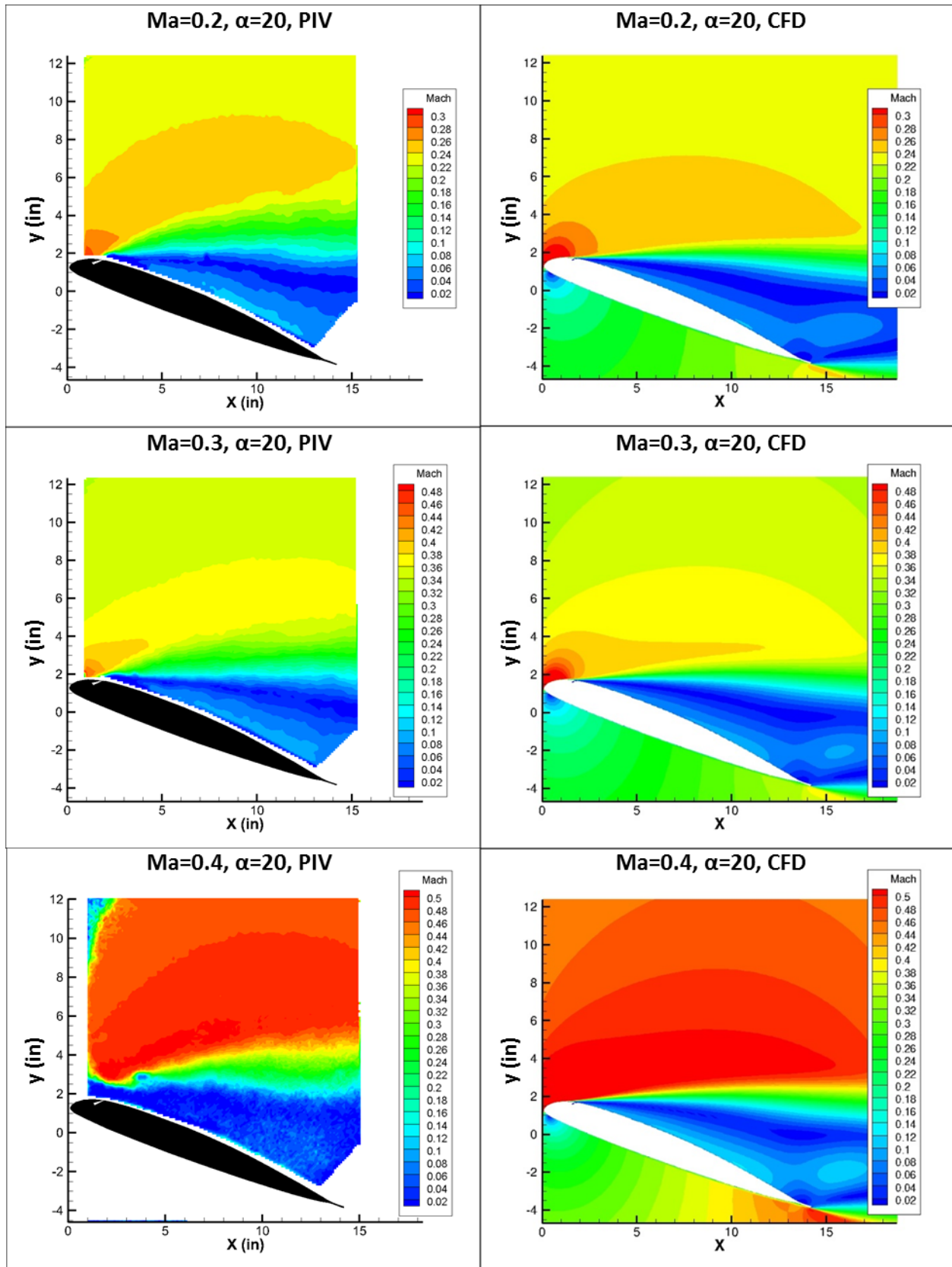
Figure 6. Velocity fields for the baseline steady airfoil. *Ma*=0.2 (top), 0.3 (middle) and 0.4 (bottom). $\alpha = 20°$. **PIV (left) and CFD (right).**
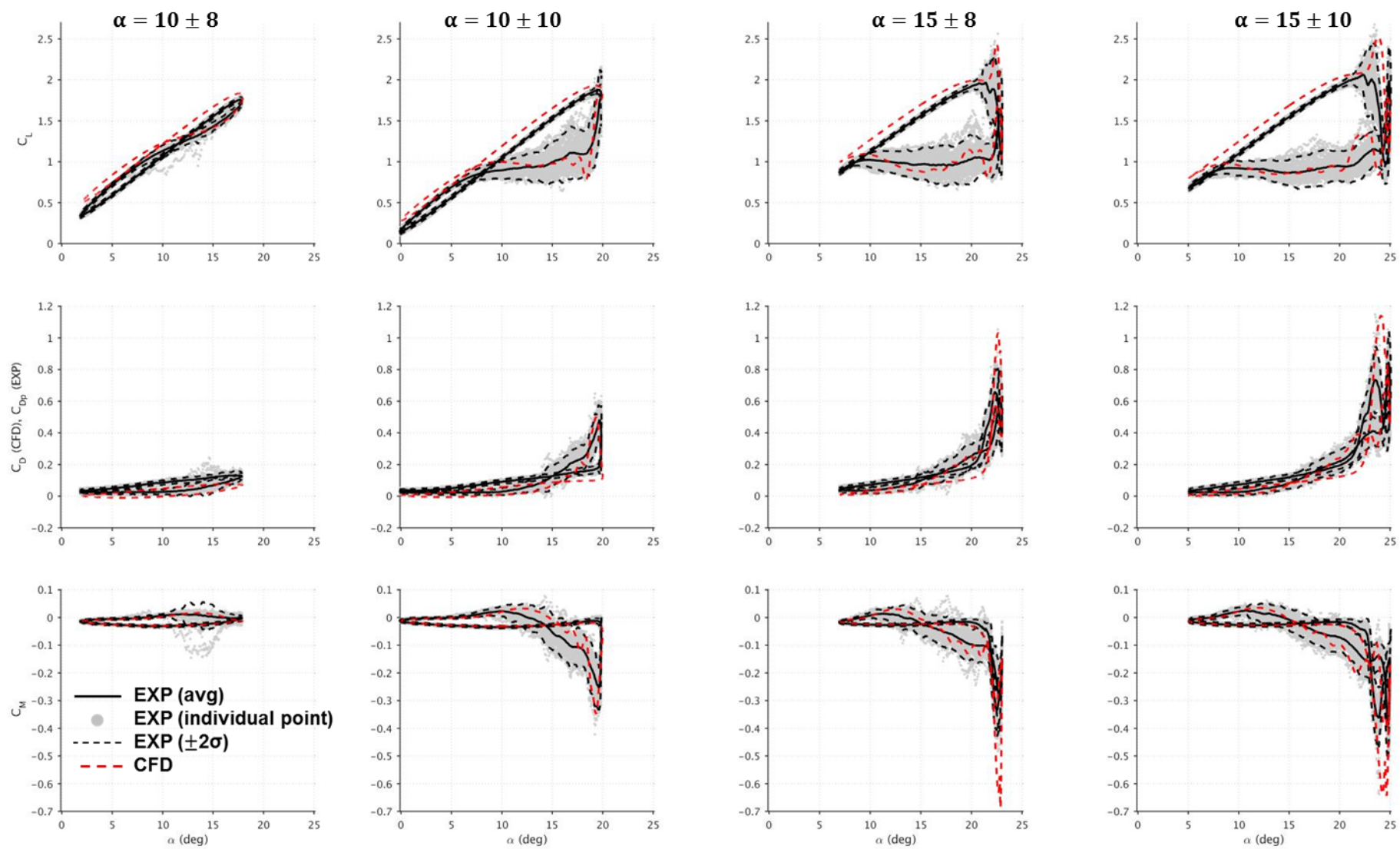
Figure 7. Aerodynamic forces for the pitching airfoil. *Ma*=0.2 and *k*=0.07.
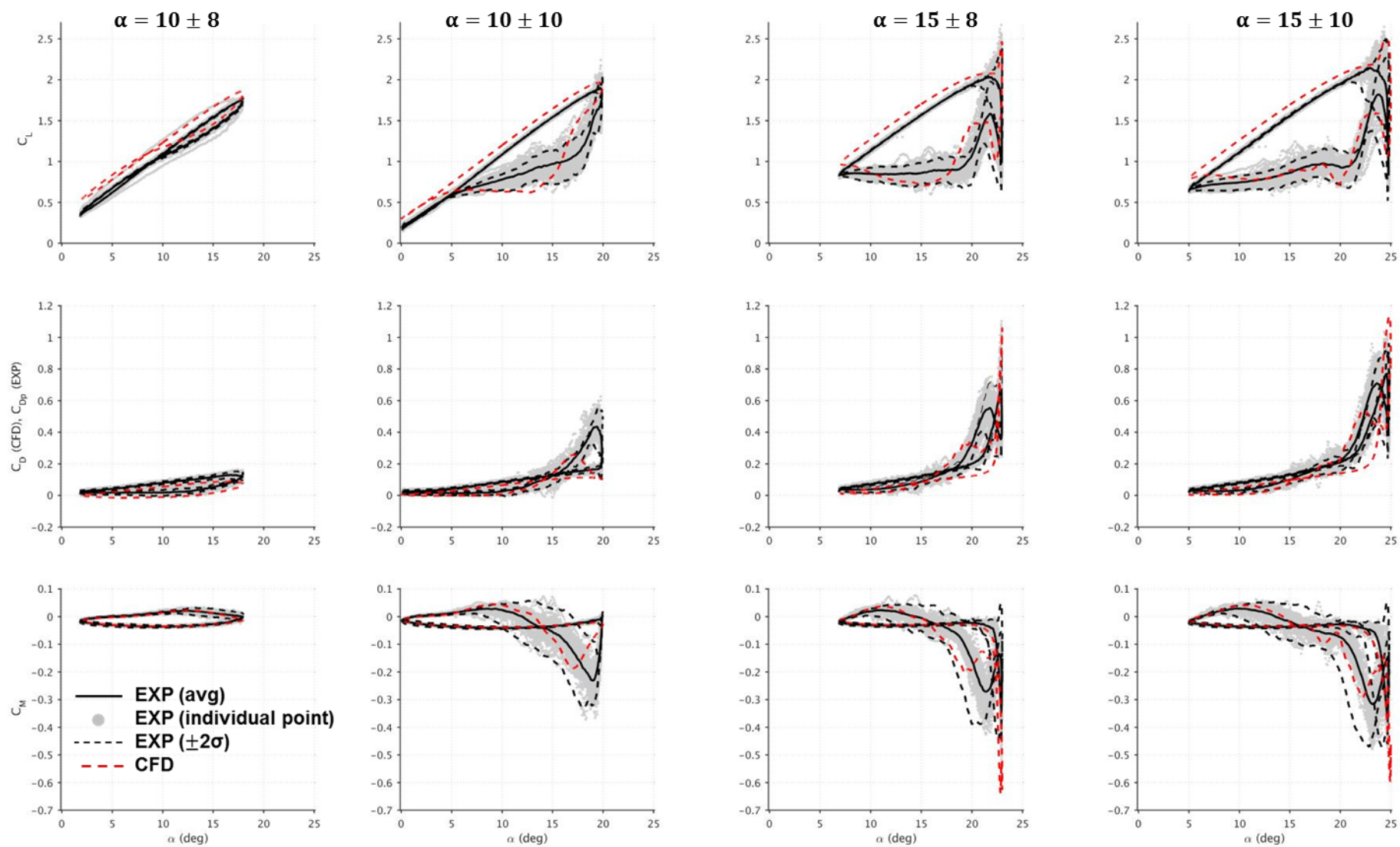
Figure 8. Aerodynamic forces for the pitching airfoil. *Ma*=0.2 and *k*=0.1.
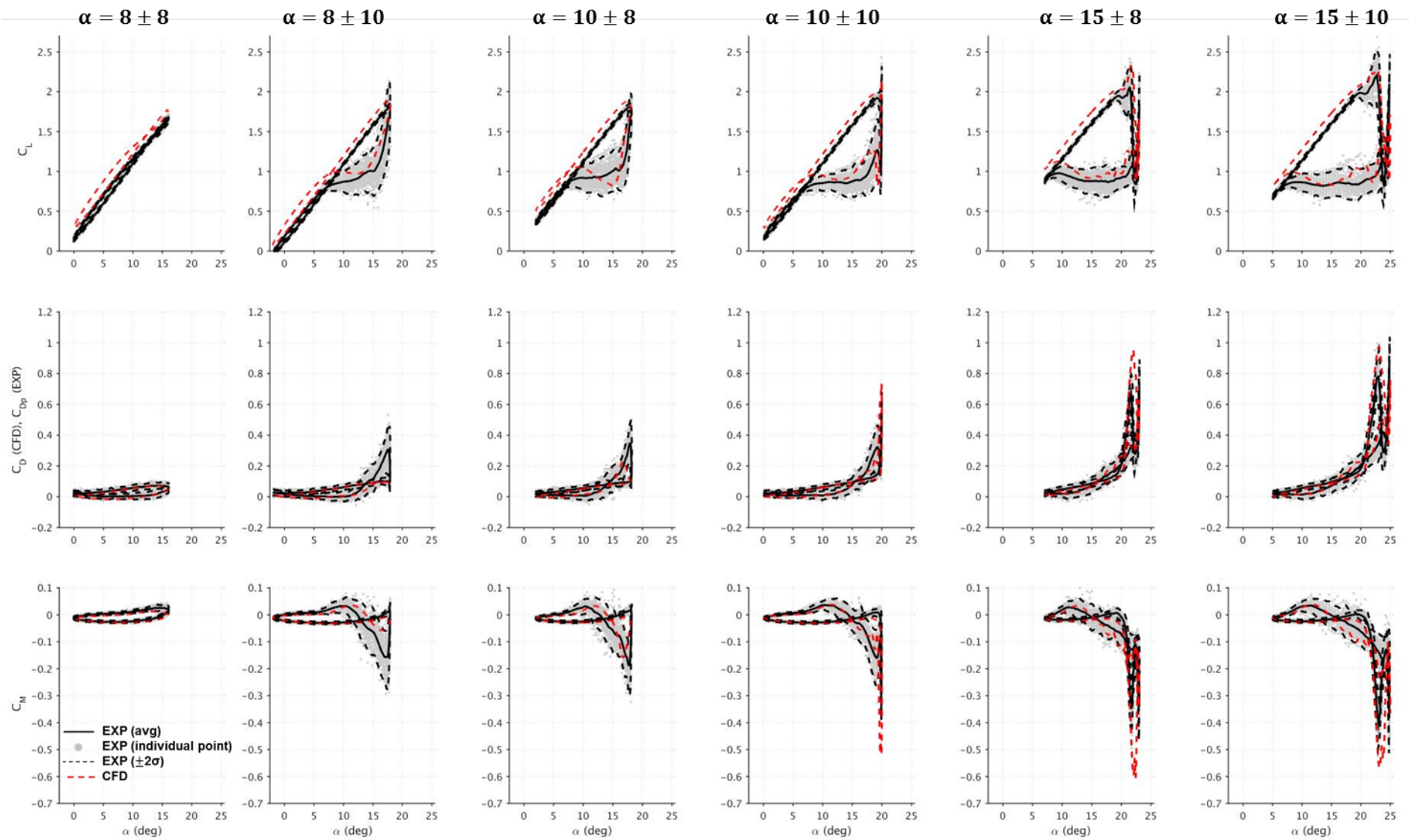
Figure 9. Aerodynamic forces for the pitching airfoil. *Ma*=0.3 and *k*=0.07.
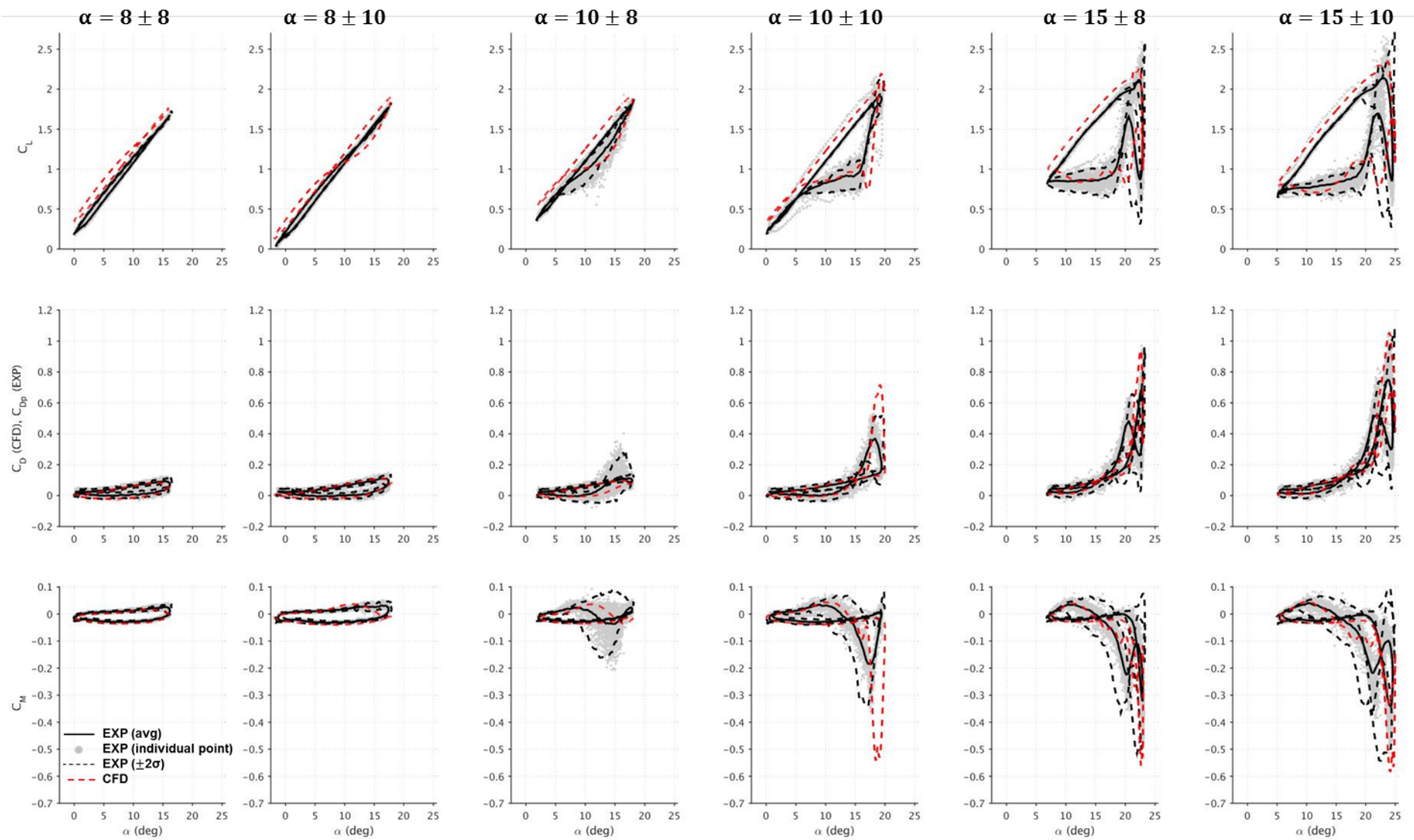
Figure 10. Aerodynamic forces for the pitching airfoil. *Ma*=0.3 and *k*=0.1.
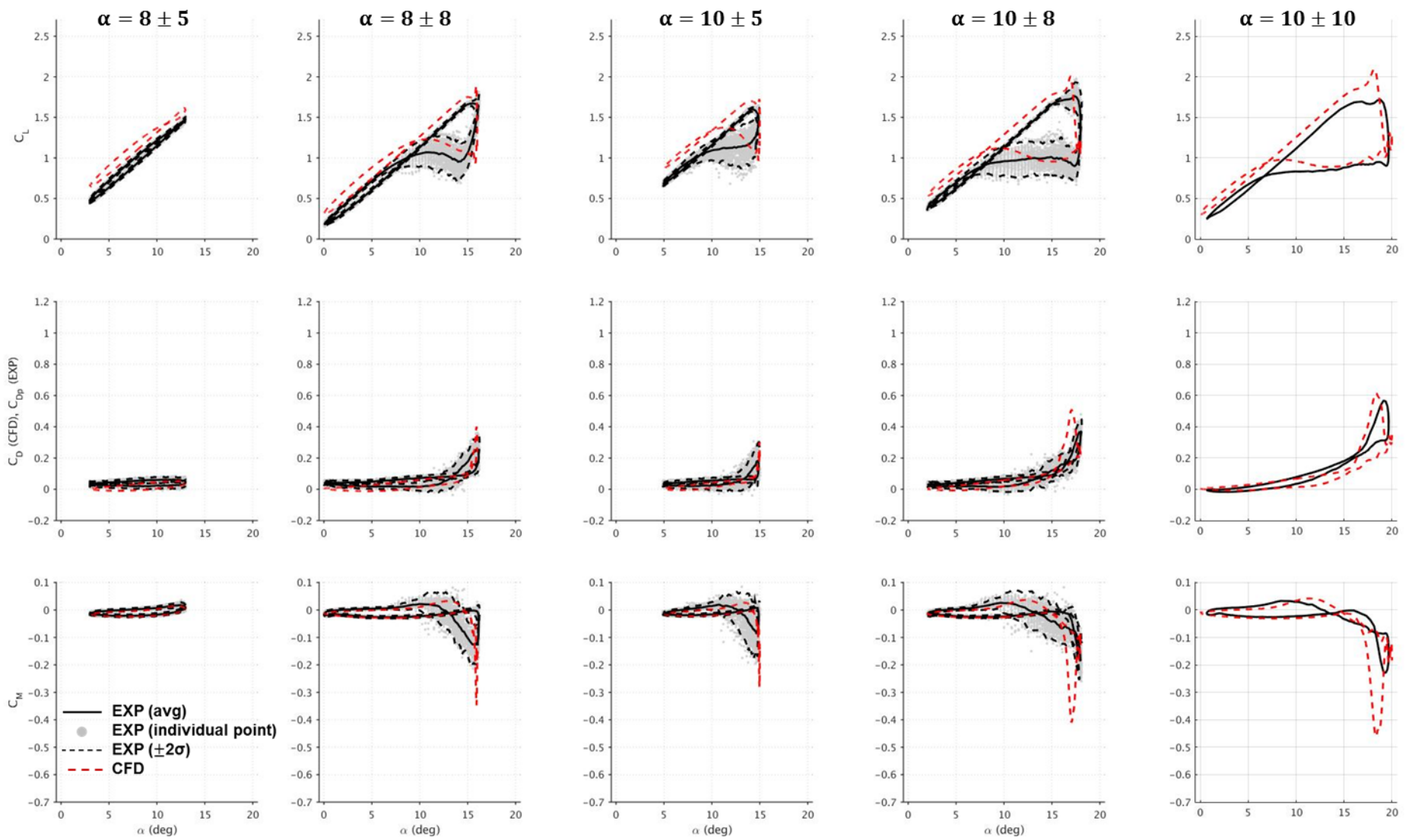
Figure 11. Aerodynamic forces for the pitching airfoil. *Ma*=0.04 and *k*=0.07.
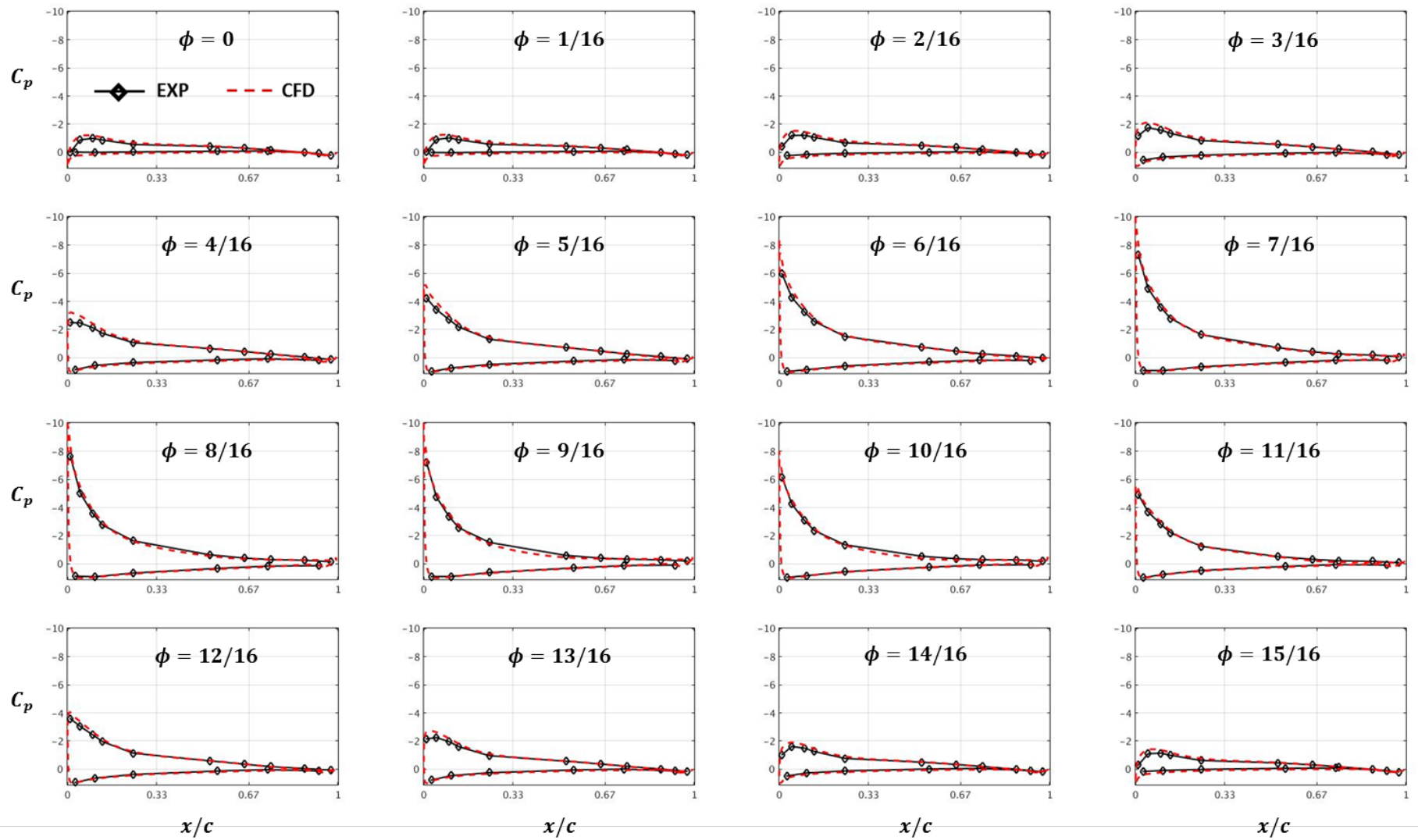
Figure 12. Pressure profiles at 16 selected phases for the baseline pitching airfoil. *Ma*=0.2, *k*=0.07 and $\alpha = 10 + 8\sin[2\pi(\phi - 1/4)]$
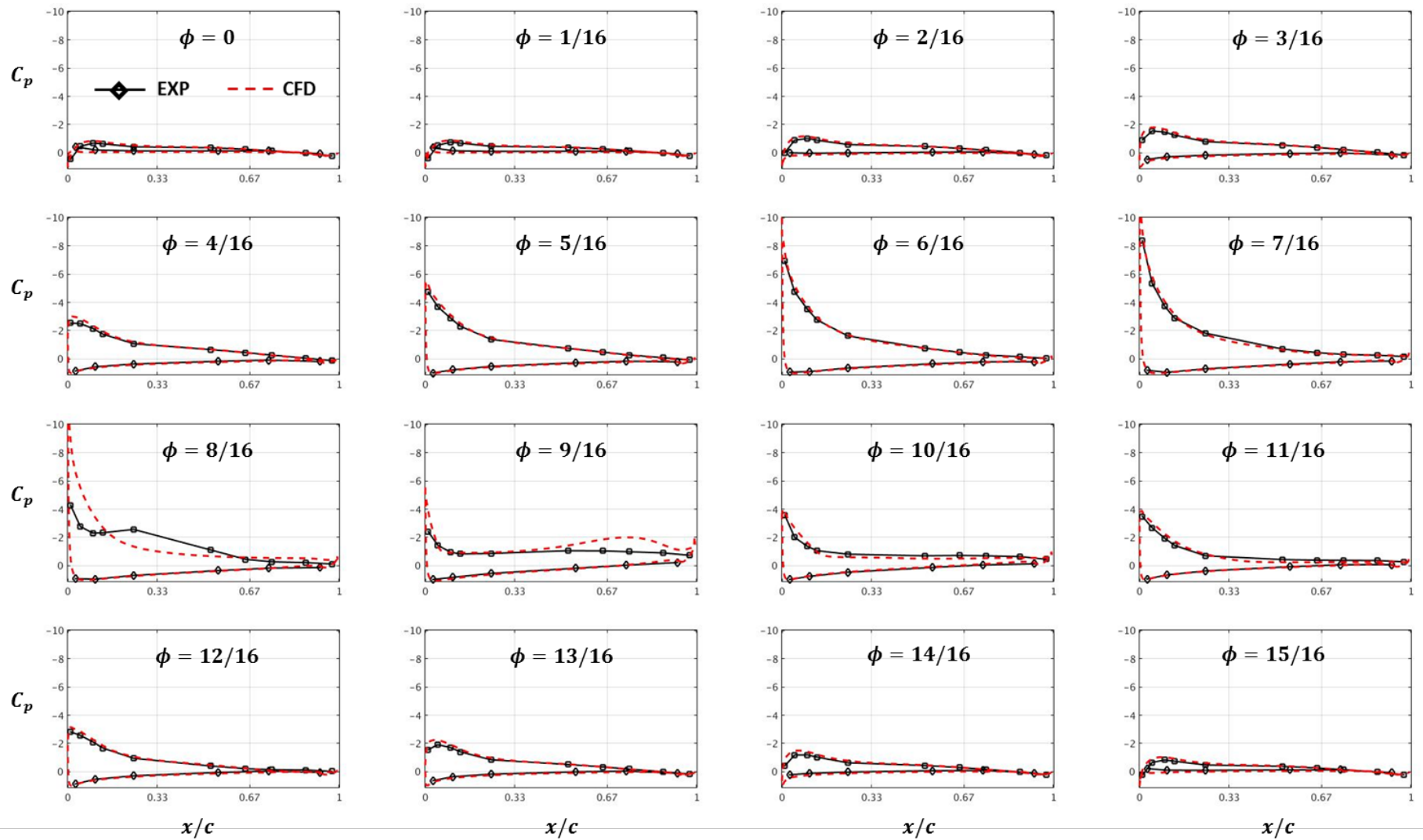
Figure 13. Pressure profiles at 16 selected phases for the baseline pitching airfoil. *Ma*=0.2, *k*=0.07 and $\alpha = 10 + 10\sin[2\pi(\phi - 1/4)]$
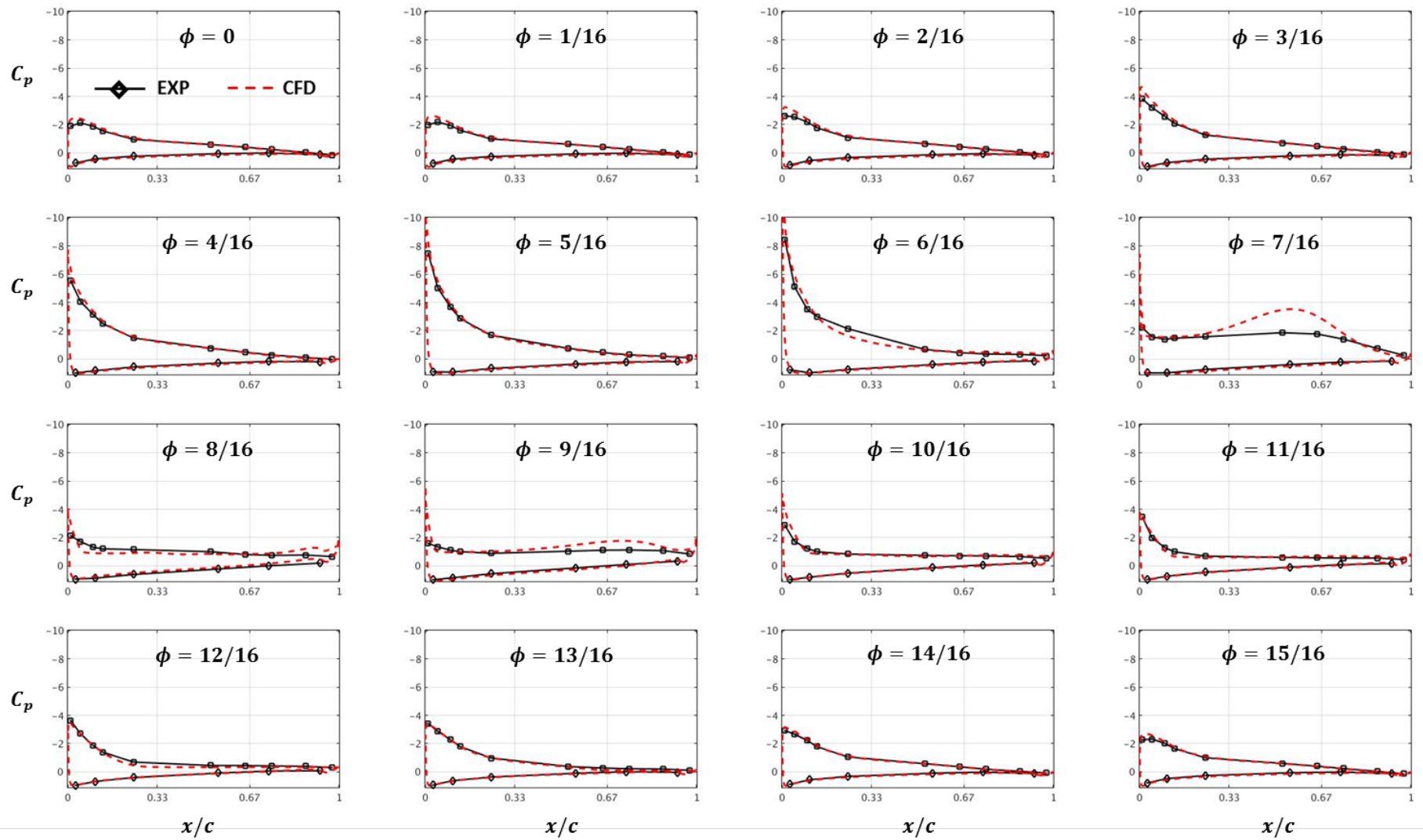
Figure 14. Pressure profiles at 16 selected phases for the baseline pitching airfoil. Ma=0.2, k=0.07 and $\alpha = 15 + 8\sin[2\pi(\phi - 1/4)]$
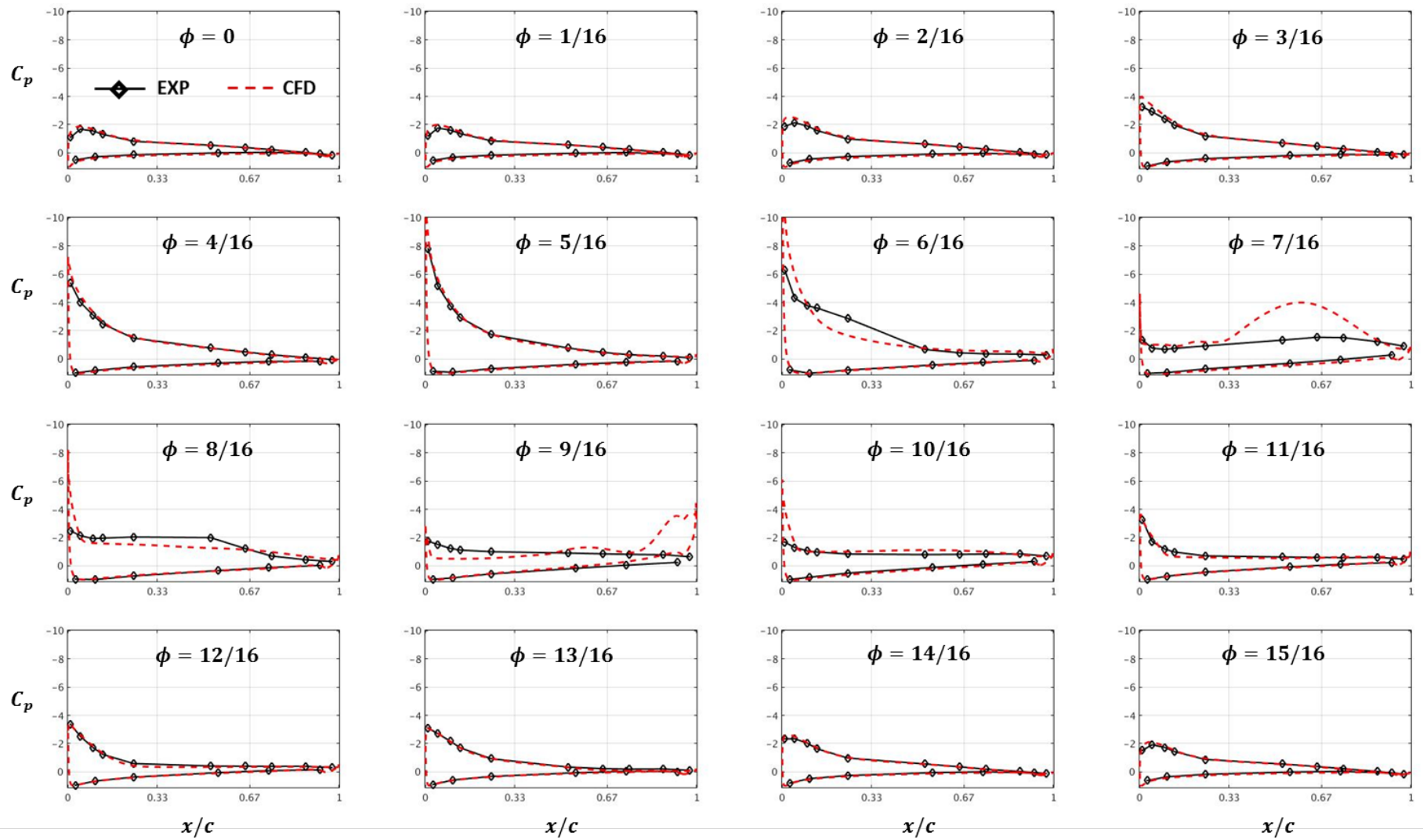
Figure 15. Pressure profiles at 16 selected phases for the baseline pitching airfoil. *Ma*=0.2, *k*=0.07 and $\alpha = 15 + 10\sin[2\pi(\phi - 1/4)]$
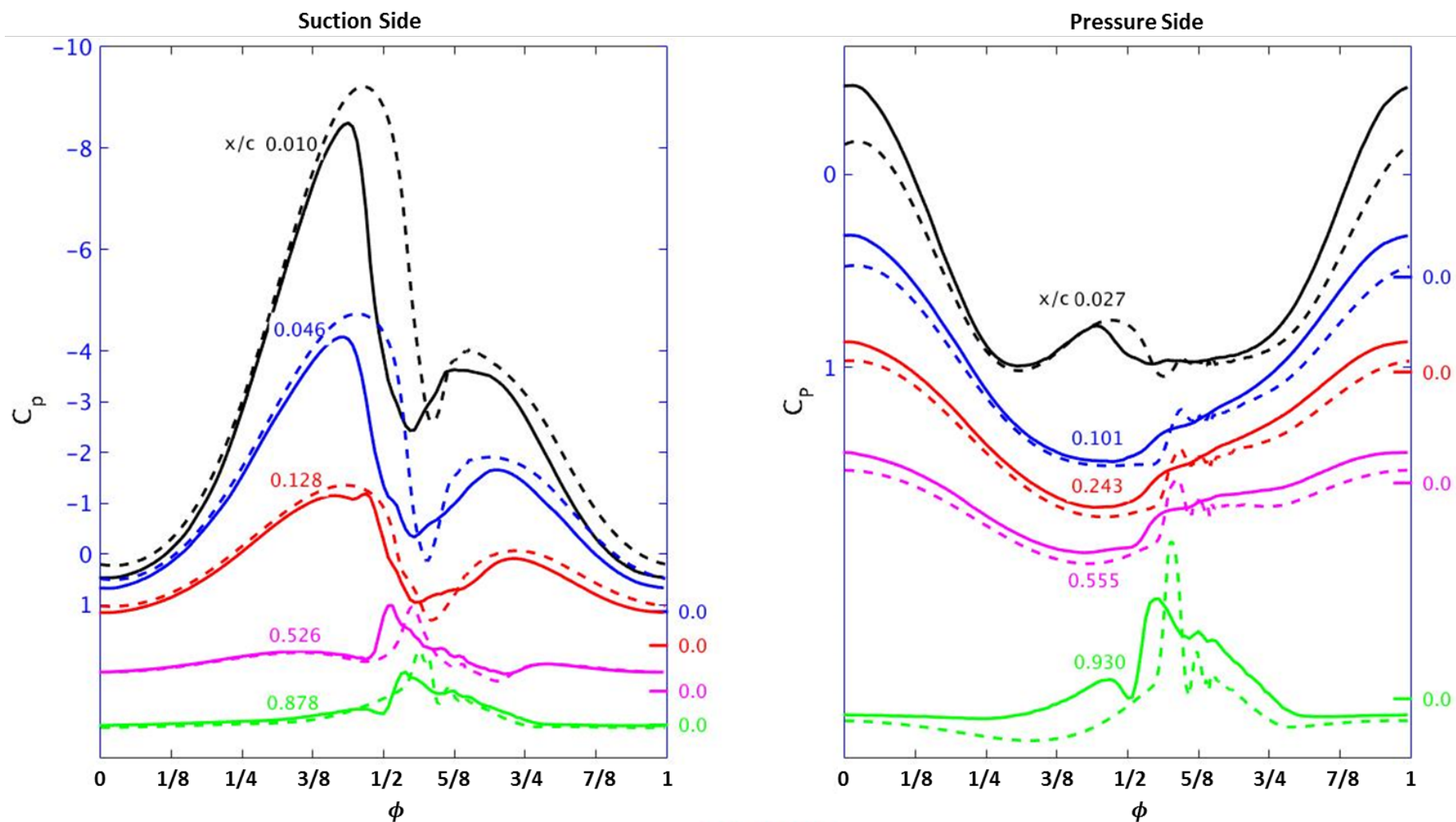
Figure 16. Stacked pressure at selected x locations for the baseline pitching airfoil. *Ma*=0.2, *k*=0.07 and $\alpha = 10 + 10\sin[2\pi(\phi - 1/4)]$. Solid lines are experimental data; dashed lines are computational data. Four downstream pressure measurements on each side are shifted from the most upstream measurement, and the zero pressure at each downstream station is notified on the right vertical axis.
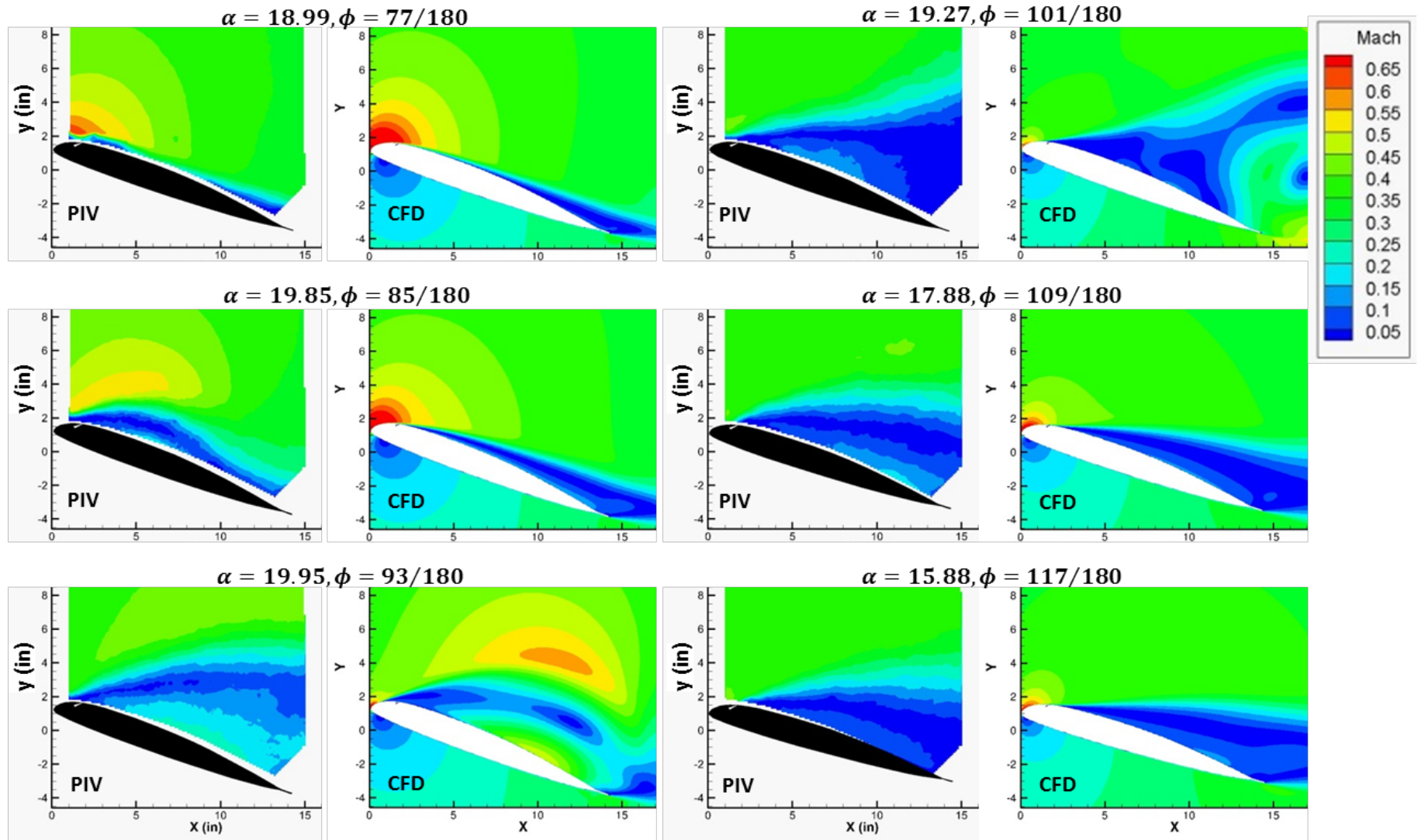
Figure 17. Velocity fields for the baseline pitching airfoil. *Ma*=0.3, *k*=0.07 and $\alpha = 10 + 10\sin[2\pi(\phi - 1/4)]$.
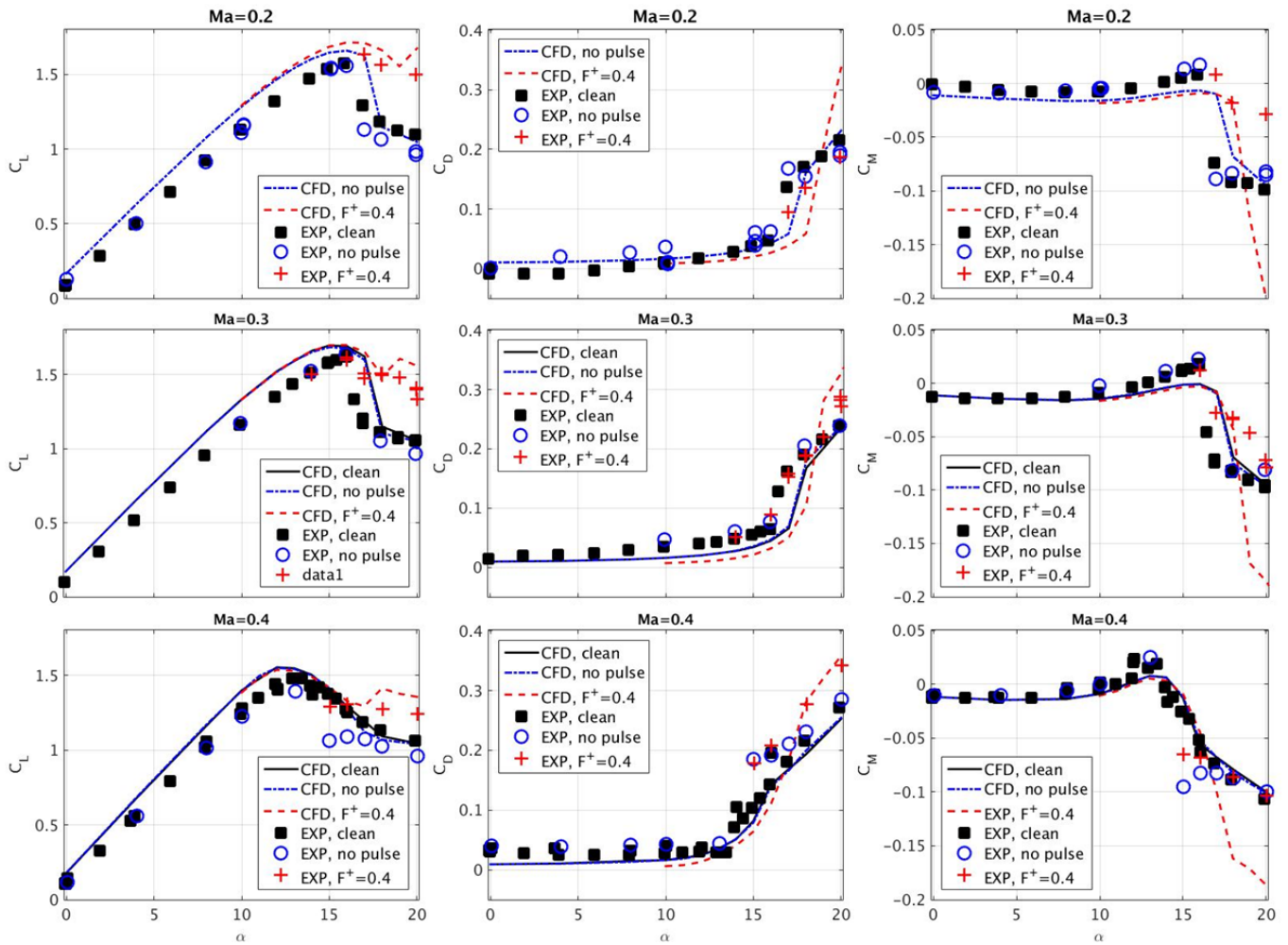
Figure 18. Aerodynamic forces for steady airfoils with and without COMPACT. *Ma*=0.2, 0.3 and 0.4. The label 'no pulse' indicates the modified VR-12 without the actuation.
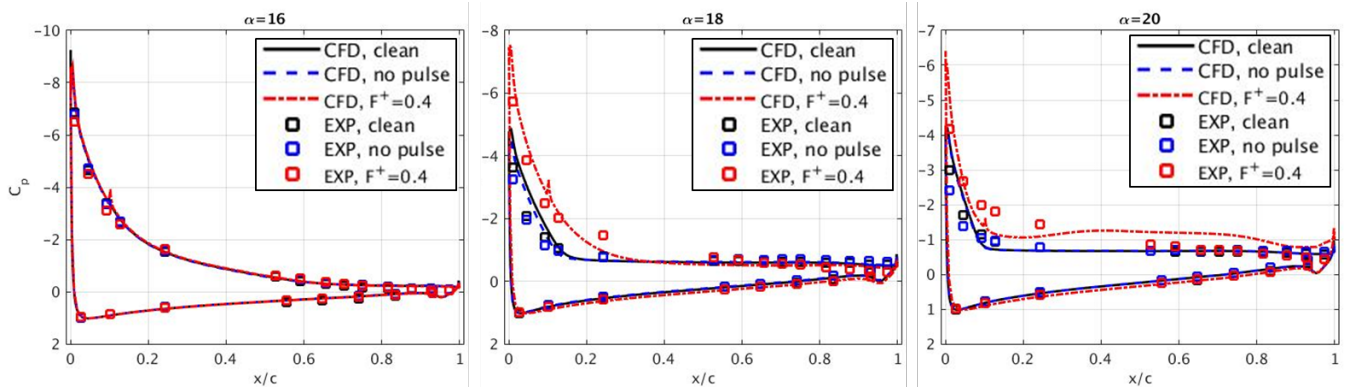
Figure 19. Pressure profiles for steady airfoils with and without COMPACT. *Ma*=0.3. The label 'no pulse' indicates the modified VR-12 without the actuation.
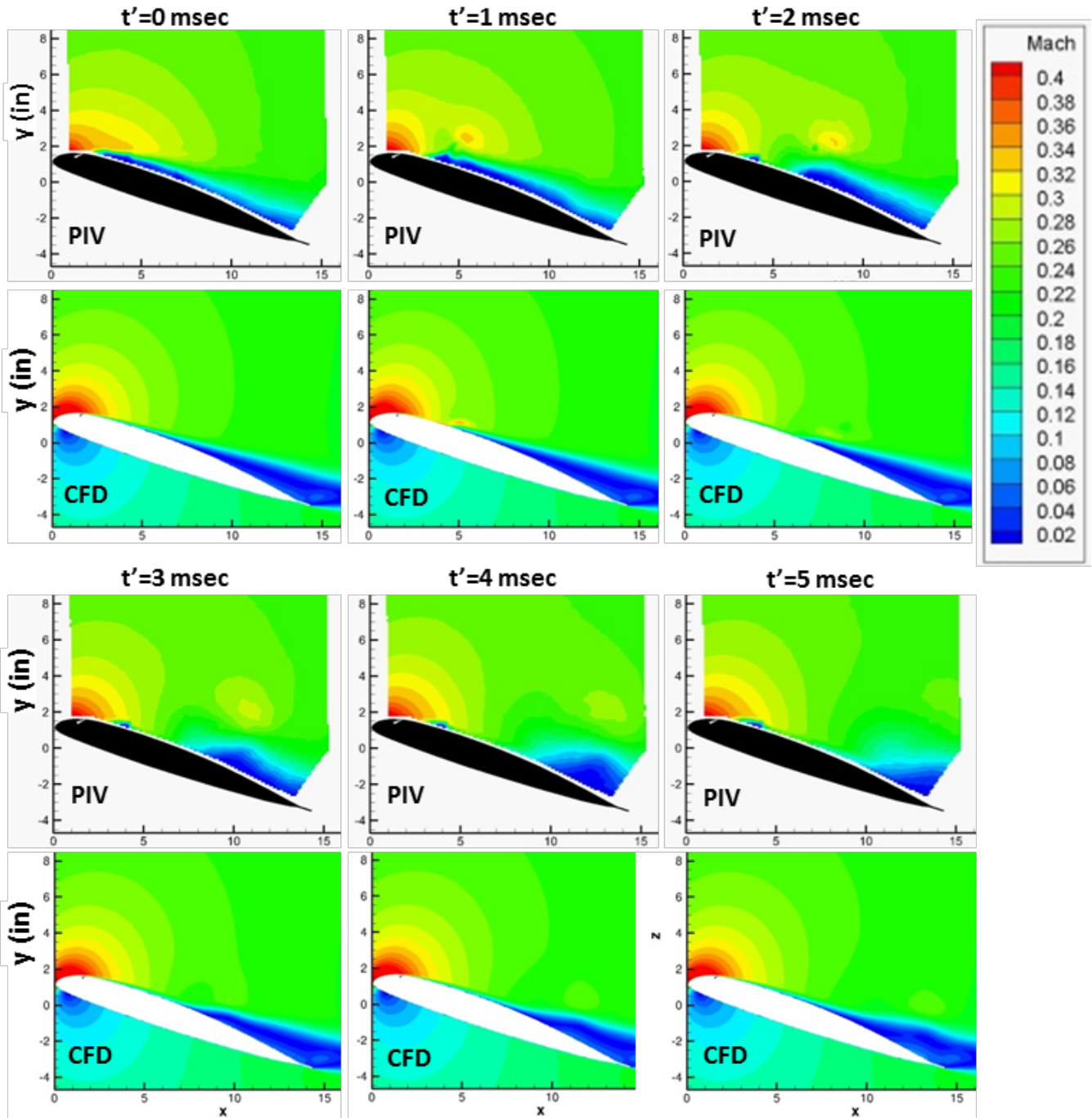
Figure 20. Velocity magnitude fields for the steady airfoil with COMPACT. *Ma*=0.2, *α*=18 and *F*⁺=0.4.
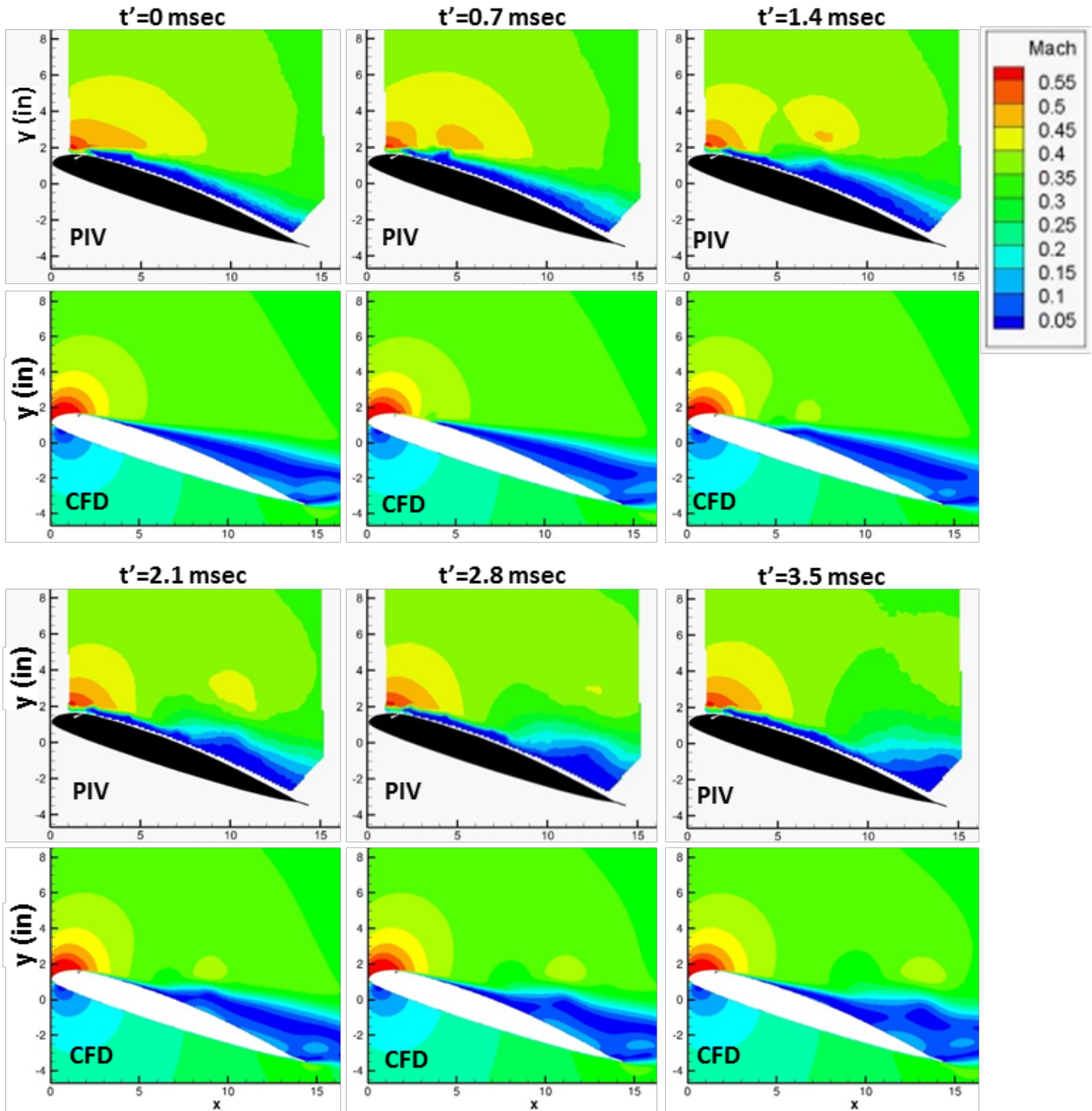
Figure 21. Velocity magnitude fields for the steady airfoil with COMPACT. Ma=0.3, α=18 and F^+=0.4.
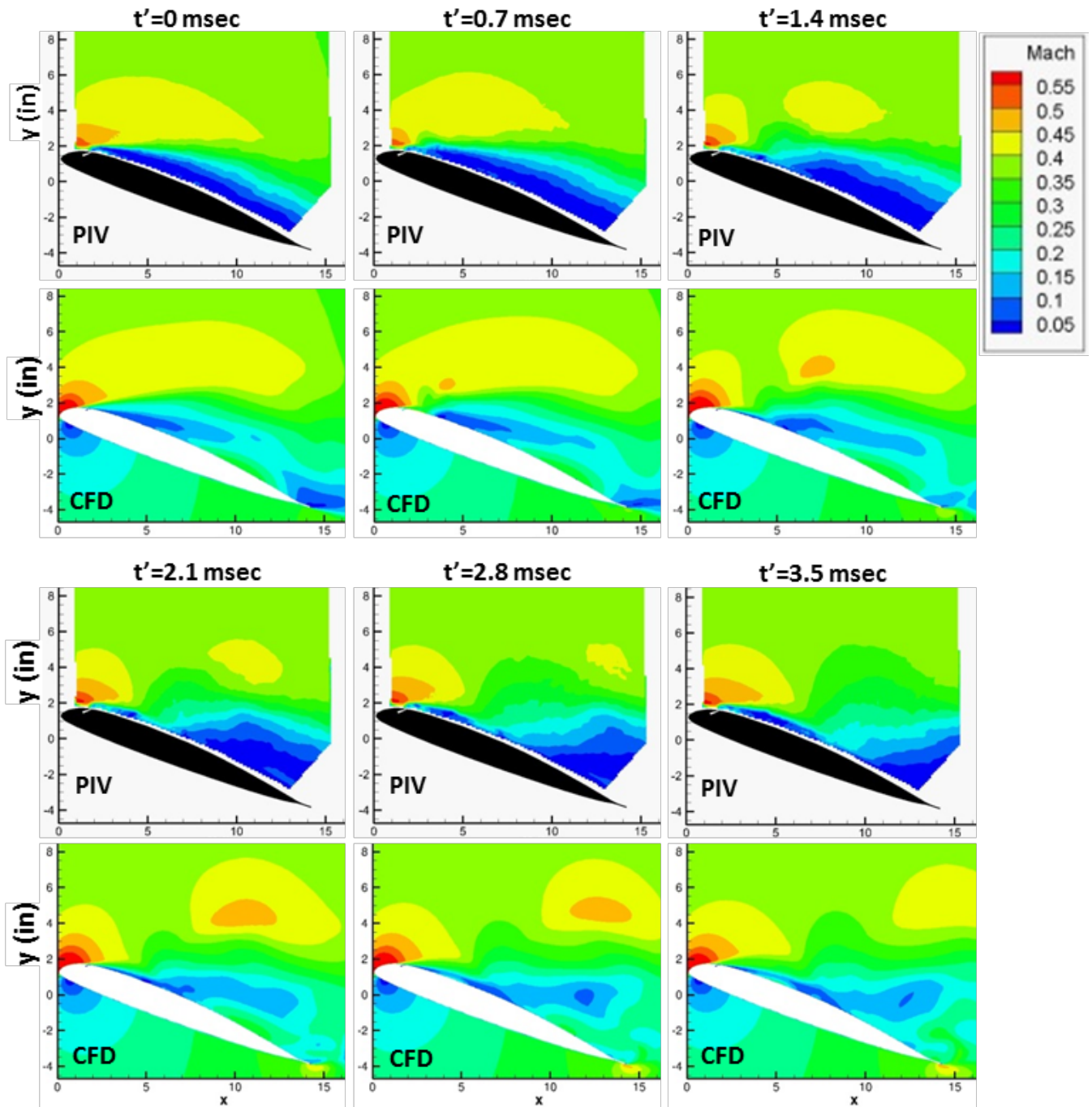
Figure 22. Velocity magnitude fields for the steady airfoil with COMPACT. Ma=0.3, α=20 and F^{+}=0.4.
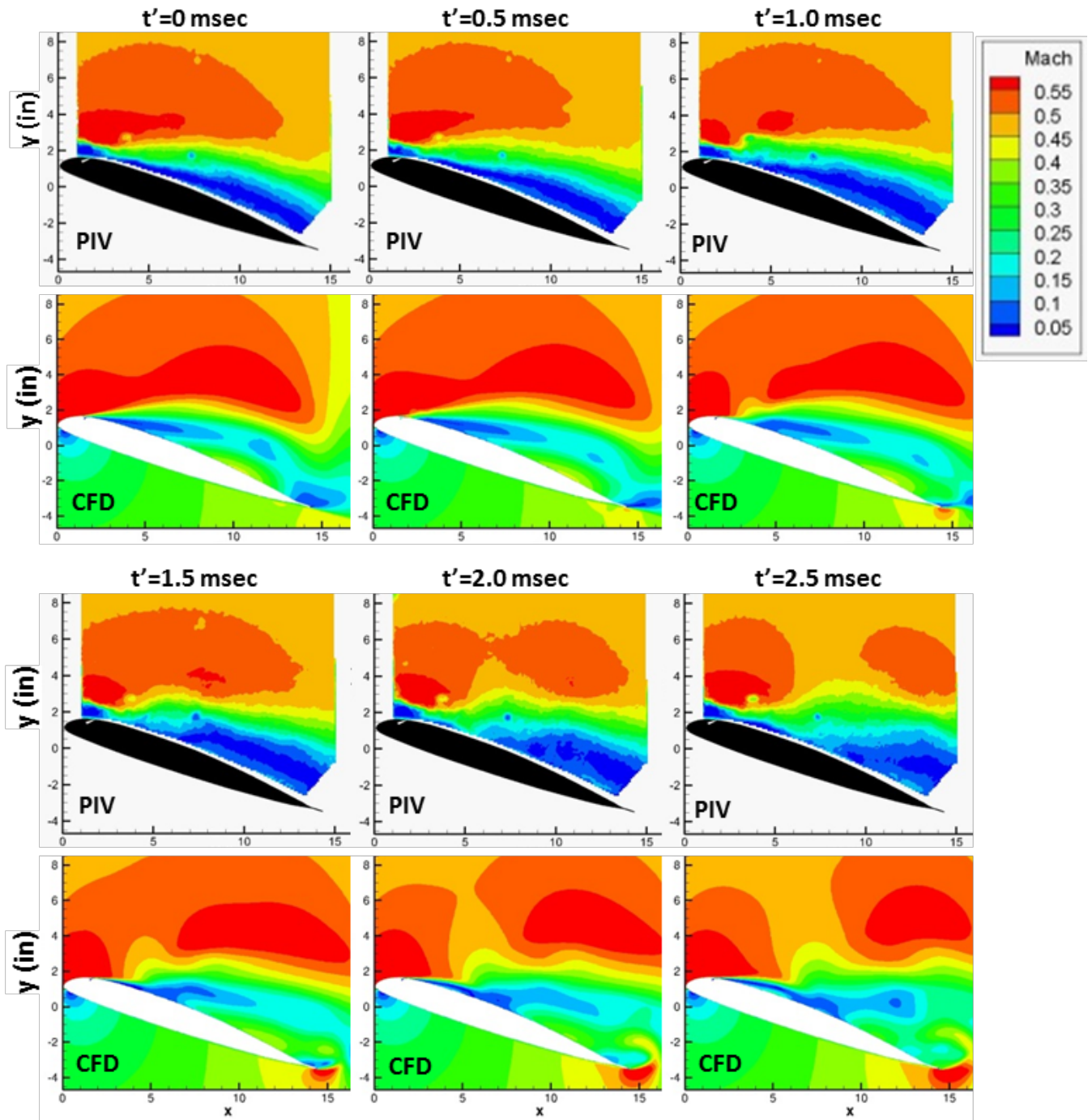
Figure 23. Velocity magnitude fields for the steady airfoil with COMPACT. *Ma*=0.4, *α*=18 and *F*⁺=0.4.
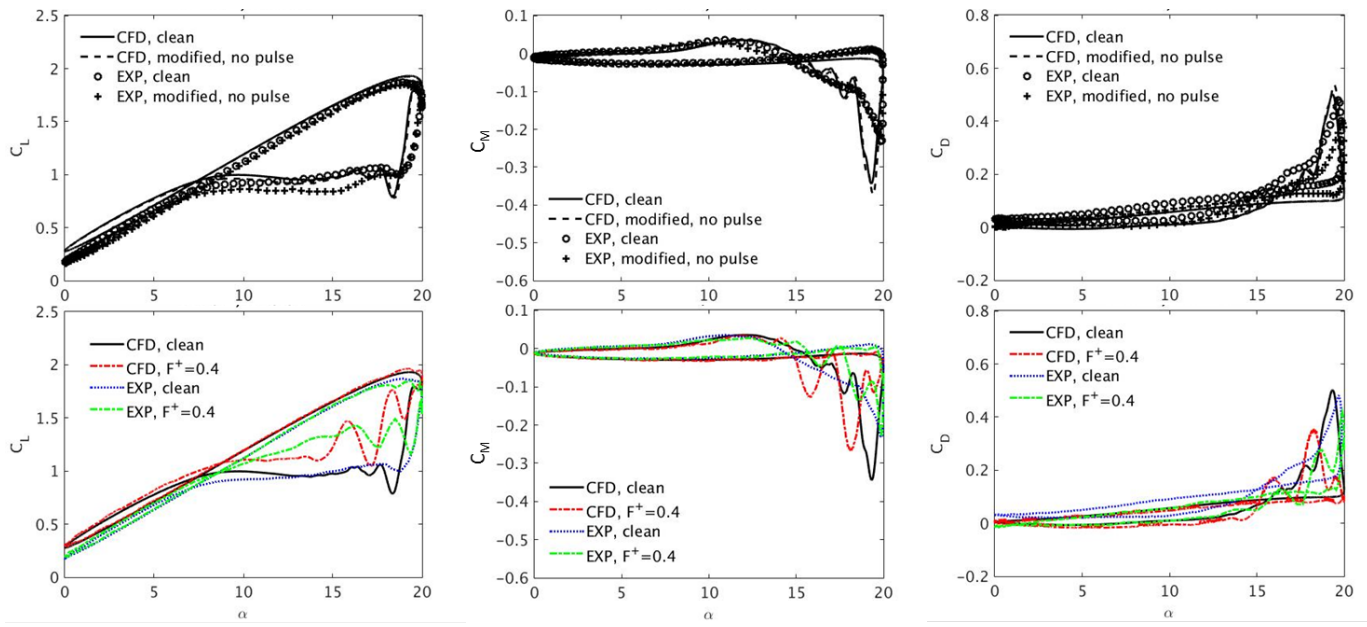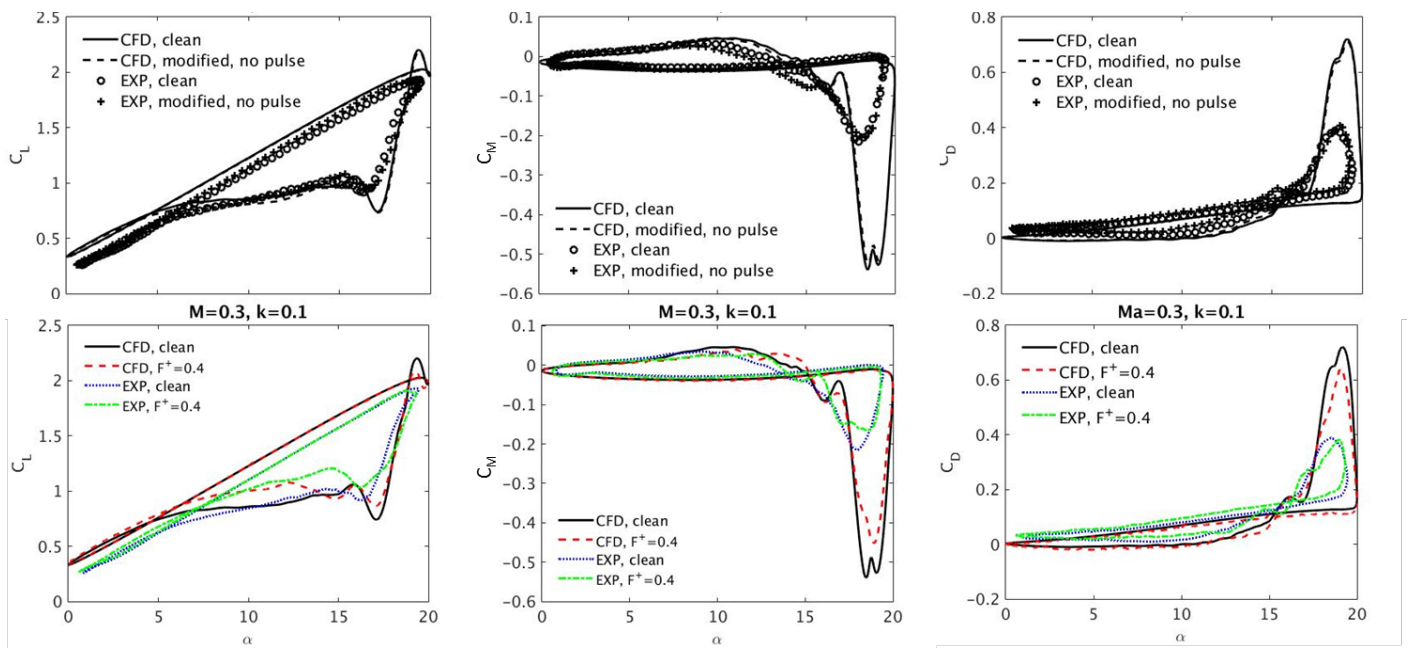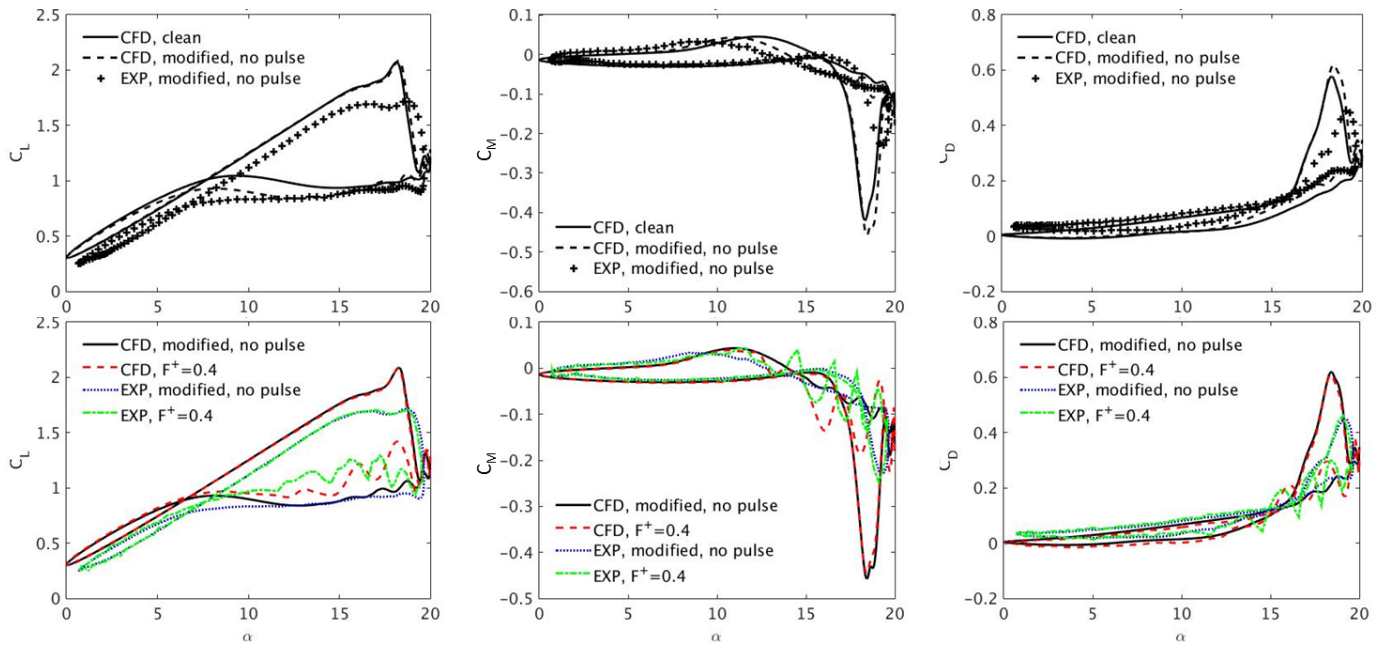
Figure 24. Aerodynamic forces for pitching airfoils with and without COMPACT. *Ma*=0.2 and *k*=0.07.
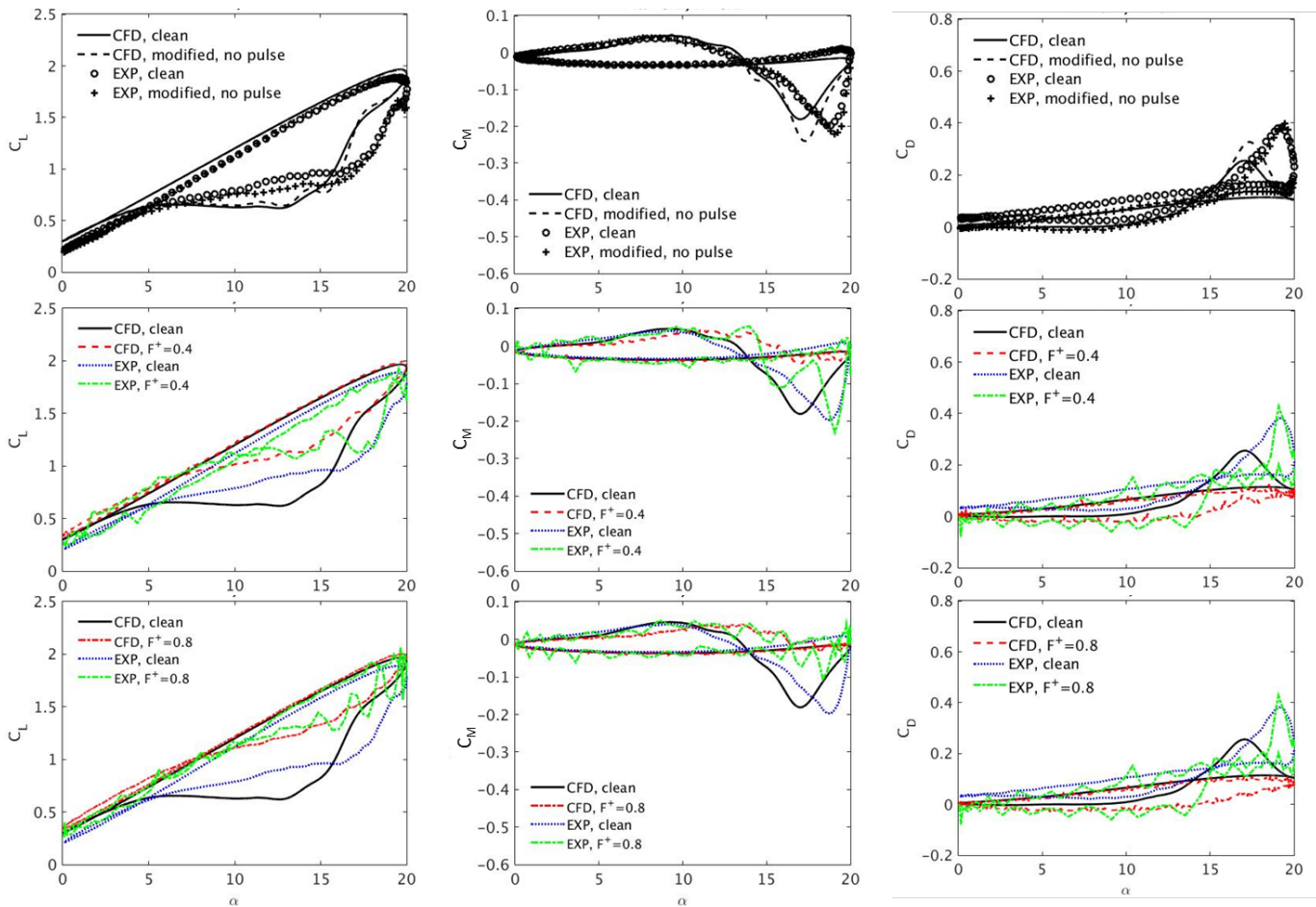
Figure 25. Aerodynamic forces for pitching airfoils with and without COMPACT. *Ma*=0.2 and *k*=0.1.
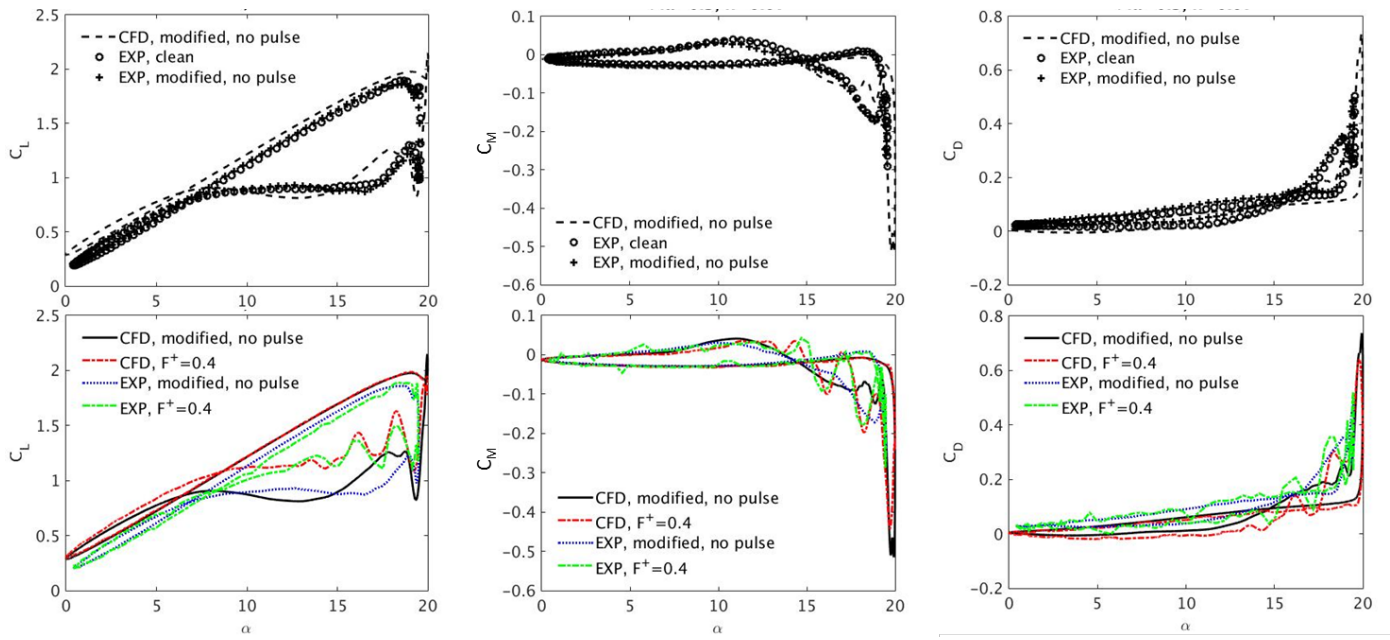
Figure 26. Aerodynamic forces for pitching airfoils with and without COMPACT. *Ma*=0.3 and *k*=0.07.

Figure 27. Aerodynamic forces for pitching airfoils with and without COMPACT. *Ma*=0.3 and *k*=0.1.

Figure 28. Aerodynamic forces for pitching airfoils with and without COMPACT. *Ma*=0.4 and *k*=0.07.
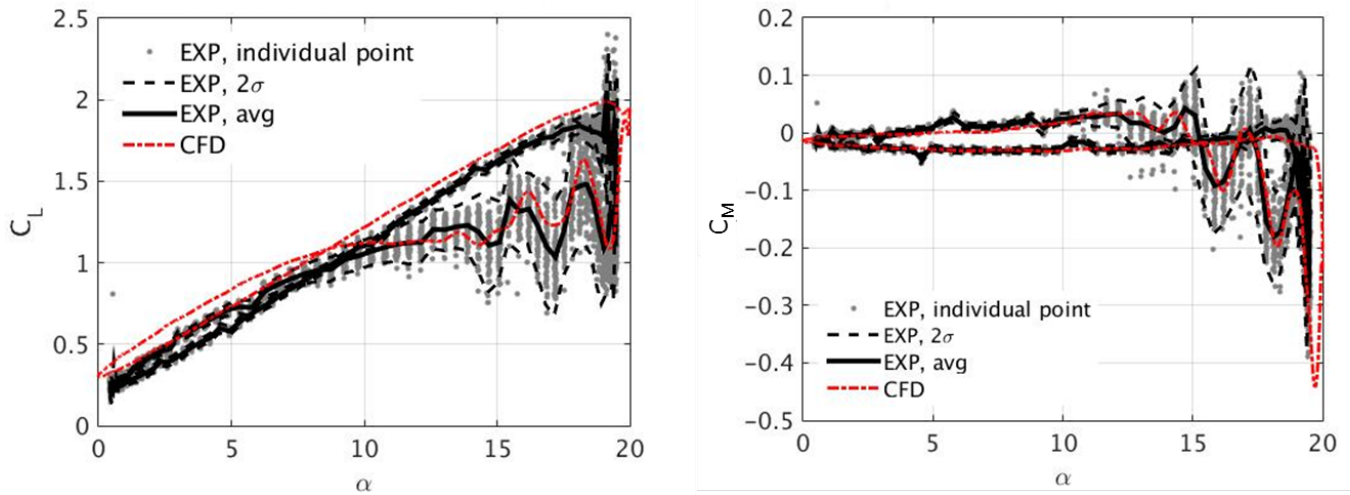

Figure 29. Aerodynamic forces for pitching airfoils with and without COMPACT. *Ma*=0.3, *k*=0.07 and *F*⁺=0.4.
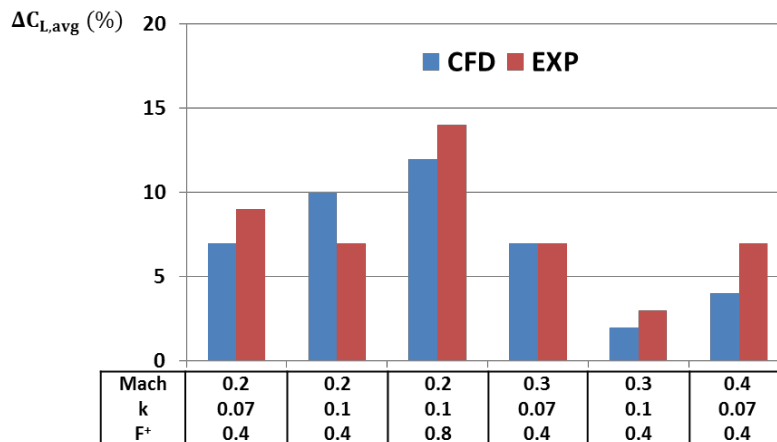

Figure 30. Baseline relative average lift increase per cycle due to COMPACT.